ELSEVIER

Journal of the Mechanics and Physics of Solids
52 (2004) 691–724

JOURNAL OF THE
MECHANICS AND
PHYSICS OF SOLIDS

www.elsevier.com/locate/jmps

Predictive modeling of nanoindentation-induced homogeneous dislocation nucleation in copper

Ting Zhu[a], Ju Li[b,d], Krystyn J. Van Vliet[c,e], Shigenobu Ogata[f,g], Sidney Yip[b,c,*], Subra Suresh[a,c]

[a] *Department of Mechanical Engineering, Massachusetts Institute of Technology, 77 Massachusetts Avenue, Cambridge, MA 02139, USA*
[b] *Department of Nuclear Engineering, Massachusetts Institute of Technology, 77 Massachusetts Avenue, Cambridge, MA 02139, USA*
[c] *Department of Materials Science and Engineering, Massachusetts Institute of Technology, 77 Massachusetts Avenue, Cambridge, MA 02139, USA*
[d] *Department of Materials Science and Engineering, Ohio State University, Columbus, OH 43210, USA*
[e] *Department of Surgery, Children's Hospital and Harvard Medical School, Boston, MA 02115, USA*
[f] *Handai Frontier Research Center, Osaka University, Osaka 565-0871, Japan*
[g] *Department of Mechanical Engineering and Systems, Osaka University, Osaka 565-0871, Japan*

Received 19 December 2002; accepted 15 July 2003

Abstract

Nanoscale contact of material surfaces provides an opportunity to explore and better understand the elastic limit and incipient plasticity in crystals. Homogeneous nucleation of a dislocation beneath a nanoindenter is a strain localization event triggered by elastic instability of the perfect crystal at finite strain. The finite element calculation, with a hyperelastic constitutive relation based on an interatomic potential, is employed as an efficient method to characterize such instability. This implementation facilitates the study of dislocation nucleation at length scales that are large compared to atomic dimensions, while remaining faithful to the nonlinear interatomic interactions. An instability criterion based on bifurcation analysis is incorporated into the finite element calculation to predict homogeneous dislocation nucleation. This criterion is superior to that based on the critical resolved shear stress in terms of its accuracy of prediction for both the nucleation site and the slip character of the defect. Finite element calculations of nanoindentation of single crystal copper by a cylindrical indenter and predictions of dislocation nucleation are validated by comparing with direct molecular dynamics simulations governed by the same interatomic potential. Analytic 2D and 3D linear elasticity solutions based on the Stroh formalism are

* Corresponding author. Department of Nuclear Engineering, Massachusetts Institute of Technology, 77 Massachusetts Avenue, Cambridge, MA 02139, USA. Tel.: +1-617-258-3809; fax: +1-617-253-8863.
E-mail addresses: syip@mit.edu (S. Yip), ssuresh@mit.edu (S. Suresh).

0022-5096/$ - see front matter
doi:10.1016/j.jmps.2003.07.006

used to benchmark the finite element results. The critical configuration of homogeneous dislocation nucleation under a spherical indenter is quantified with full 3D finite element calculations. The prediction of the nucleation site and slip character is verified by direct molecular dynamics simulations. The critical stress state at the nucleation site obtained from the interatomic potential is in quantitative agreement with ab initio density functional theory calculation.

Keywords: Nanoindentation; Dislocation nucleation; Finite element; Hyperelasticity; Cauchy–Born hypothesis; Molecular dynamics

1. Introduction

Nanoscale contact of material surfaces provides an opportunity to explore and better understand the elastic limit and incipient plasticity in crystals. A common mode of instability at the elastic limit of a perfect crystal is strain localization, resulting ultimately in the homogeneous nucleation of crystalline defects such as dislocations (Hill, 1975; Rice, 1976; Xu and Argon, 2001). In load-controlled nanoindentation experiments, after a preliminary elastic stage, a discontinuity in indenter displacement has been captured for the measured load P versus indentation depth h response for several cubic crystals (Page et al., 1992; Oliver and Pharr, 1992; Gerberich et al., 1996; Corcoran et al., 1997; Suresh et al., 1999; Gouldstone et al., 2000). The onset of this displacement discontinuity is thought to indicate that atomically localized deformation, i.e. dislocation nucleation occurs beneath the indenter. Recent in situ experiments by Gouldstone et al. (2001) using the Bragg–Nye bubble raft as an analogue to the $\{1\,1\,1\}$ plane of face-centered cubic (FCC) crystal clearly demonstrated that nanoindentation of a two-dimensional crystal may lead to homogeneous nucleation of dislocations within the crystal. Atomistic simulations by Tadmor et al. (1999a) via the quasicontinuum method revealed the process of nanoindentation-induced dislocation nucleation near the surface in single crystal aluminum. However, a quantitative understanding of the critical condition for homogeneous dislocation nucleation is still lacking. An accurate characterization of defect nucleation serves two purposes in multiscale materials modeling. First, a reliable defect nucleation criterion can be extracted to seed the initial defect distribution and originate new defects in mesoscopic dislocation dynamics simulations (Fivel et al., 1998; Shenoy et al., 2000). Second, quantum mechanical ideal strength calculations that reveal bonding and electronic structure characteristics (Krenn et al., 2001; Ogata et al., 2002) can be connected with the experimental nanoindentation P–h response. Specifically, as ab initio calculations are computationally intensive, we may rely on an empirical interatomic potential to identify the nucleation site and the critical stress state, and then analyze the corresponding electronic structure characteristics using ab initio calculations. As a continuing effort of predictive modeling of defect nucleation (Li et al., 2002; Van Vliet et al., 2003), in this paper we present an atomistically faithful characterization of the critical condition of contact-induced homogeneous dislocation nucleation, based on three essential elements: (1) a computationally efficient continuum method to perform simulations with experimentally relevant length/time scales; (2) an

atomistically verified instability criterion to predict dislocation nucleation; and (3) an optimally parameterized interatomic potential to model the constitutive response.

Finite strain elastic instability of perfect crystal during nanoindentation can be studied using either an atomistic or a continuum approach. The most detailed information beneath the indenter is revealed by direct molecular dynamics (MD) simulations (Kelchner et al., 1998; Zimmerman et al., 2001). However, due to the computational cost associated with keeping track of large number of atoms, the physical length and time scales for MD simulations are very limited. In contrast, continuum-level finite element method (FEM) calculations with a hyperelastic constitutive relation based on an interatomic potential represent a computationally efficient method to study nonlinear instability at comparatively larger length scales and for realistic boundary conditions, into which crystallographic and nonlinear (de)bonding features of the underlying lattice can be incorporated. The basic premise of this approach is that every point in a continuum corresponds to a large, uniformly deformed region at the atomic scale. Hence the constitutive relation for each continuum point can be derived within the framework of hyperelasticity with the Cauchy–Born hypothesis (Born and Huang, 1956; Ericksen, 1984; Tadmor et al., 1996; Ortiz and Phillips, 1999; Abeyaratne et al., 2001). This hypothesis states that the Bravias lattice vectors deform according to the macroscopic deformation gradient. Based on this geometrical connection, one can calculate the local continuum stress by deforming the underlying crystal structure according to the local, atomically uniform deformation gradient, and resorting to the virial sum of interatomic forces (Born and Huang, 1956; Wallace, 1972; Allen and Tildesley, 1987). Since the constitutive relation is obtained directly from the atomic lattice sum and interatomic potential, key properties of the crystal such as crystalline anisotropy and nonlinear elastic effects are incorporated automatically. This approach describes the crystal behavior well as long as the spatial variation of deformation is not too large on the atomic scale; it will break down near defects where non-local effects become significant. Interatomic potential-based hyperelasticity is a full-continuum model and represents the local limit of the more general continuum-atomistic framework of the quasicontinuum method (Tadmor et al., 1996, 1999b; Ortiz and Phillips, 1999; Shenoy et al., 1999; Knap and Ortiz, 2001). However, for the present investigation of nanoindentation-induced elastic instability, deformation is approximately uniform at the atomic scale—though it varies significantly on the macroscale—and thus it is adequate to describe the crystal behavior accurately (Li et al., 2002; Van Vliet et al., 2003). Interatomic potential-based hyperelasticity is significantly more straightforward to implement within any general-purpose FEM package than the more flexible and thus more complex quasicontinuum approach. In this framework, quantitative prediction of defect nucleation may be achieved with the aid of an accurate and reliable defect nucleation criterion.

From the viewpoint of multiscale material modeling, one of the most useful insights that could be gained from atomistic analyses of nanoindentation is the criterion for defect nucleation. A physically rigorous criterion is much needed to replace ad hoc criteria that one must otherwise adopt, such as a critical resolved shear stress (CRSS)-based criterion. It is tempting to postulate that the critical stress a perfect crystal can sustain is a robust material constant. We believe this is not the case because the value of critical stress for the criterion depends on other stress components than just the shear

stress component acting on the plane. Density functional theory (DFT) calculations (Ogata et al., 2002) have shown that the ideal shear strength of a Cu perfect crystal depends strongly on other components of the stress. The ideal shear strength of FCC simple metals is defined as the maximum shear stress that the crystal can sustain when sheared on the $\{1\,1\,1\}$ plane in the positive $\langle 1\,1\,\bar{2}\rangle$ direction. For Cu, the DFT results by Ogata et al. (2002) gave the maximum shear stress as 2.16 GPa for relaxed shear (all stress components except the principal shear stress are zero) and 3.42 GPa for unrelaxed shear (all strain components except the principal shear strain are zero). This shows that the value of the maximum shear stress depends on specifying the full local stress environment of the nucleation site. Furthermore, the detailed study of dislocation nucleation by Shenoy et al. (2000) indicated that the stress-based nucleation criterion is able to capture only the qualitative features of the instability point induced via nanoindentation. A significant quantitative difference is found between their stress-based predictions and atomistic simulations. This is another piece of evidence pointing to the limitations of the CRSS-based criterion for predicting homogeneous dislocation nucleation under various loading conditions.

In this study, a localization criterion based on bifurcation analysis with atomistic interactions will be employed to predict nanoindentation-induced dislocation nucleation. This criterion was first proposed by Hill (1962, 1975). He showed that the loss of strong ellipticity in the strain energy function is an indication of the instability in a solid. A review of localization analysis and its application for various types of continuum inelastic material models was given by Rice (1976). Several recent studies demonstrated the applicability of this criterion in the atomically-informed continuum model where the link between the movement of atoms and the deformation of the continuum was made via the Cauchy–Born hypothesis. For example, Gao and Klein (1998), Klein and Gao (1998), and Zhang et al. (2002) applied this localization criterion to detect strain localization for virtual internal bond (VIB) material models, by which the cohesive interactions between the material particles are incorporated into the constitutive law with recourse to the Cauchy–Born hypothesis. Van Vliet et al. (2003) used this criterion to detect dislocation nucleation in 2D simulations of nanoindentation in a model material characterized by a generic interatomic potential. As shown in the following section, the application of this localization criterion requires knowledge of the nonlinear stresses and elastic moduli, which can be readily and rigorously calculated within the framework of interatomic potential-based hyperelasticity. Given these atomically informed continuum quantities, this energy-based instability criterion is an effective tool to predict defect nucleation within a crystal, as it can identify the location, character, and stress state required for homogeneous nucleation of a crystalline defect.

The outline of the paper is as follows. In Section 2, the formulation of hyperelasticity which incorporates embedded atom model (EAM) interatomic potentials is developed within the framework of continuum mechanics. Next, the elastic instability criterion for defect nucleation is formulated, and the accuracy of EAM potentials is verified by comparison with ab initio electronic structure calculations. In Section 3, the analytic solutions for frictionless indentation on a linear anisotropic elastic, single crystal half-space are given for both 2D and 3D loading configurations based on

the Stroh formalism, and analytic insights are used to rationalize the finite element simulations. In Section 4, the 2D finite element simulations of nanoindentation based on hyperelasticity and predictions of dislocation nucleation by the instability criterion are validated via comparison with molecular dynamics simulations. The critical state of nanoindentation-induced dislocation nucleation is quantified with full 3D finite element simulations in Section 5, and discussions and concluding remarks are presented in Section 6.

2. Interatomic potential-based hyperelasticity of crystalline solids

2.1. Formulation

An interatomic potential-based constitutive relation can be derived within the framework of hyperelasticity with the Cauchy–Born hypothesis (Born and Huang, 1956; Ericksen, 1984; Tadmor et al., 1996; Ortiz and Phillips, 1999; Abeyaratne et al., 2001). In continuum mechanics, we may identify a stress-free configuration denoted by $\mathscr{A}$. The current deformed configuration is denoted by $\mathscr{B}$. A line element $d\mathbf{x}_{\mathscr{A}}$ in configuration $\mathscr{A}$ is deformed into a line element $d\mathbf{x}_{\mathscr{B}}$ in configuration $\mathscr{B}$ by the macroscopic deformation gradient $\mathbf{F} \equiv \partial \mathbf{x}_{\mathscr{B}}/\partial \mathbf{x}_{\mathscr{A}}$. A fundamental postulate of hyperelasticity is the existence of a strain energy function, e.g., Ogden (1984). Then, the symmetric second Piola–Kirchhoff stress is defined by

$$\mathbf{S}^{\mathrm{PK2}} \equiv \frac{\partial \Psi}{\partial \mathbf{E}}, \tag{1}$$

with $\mathscr{A}$ as the reference configuration, where Ψ is the strain energy density function (per unit stress-free volume) and the Green strain $\mathbf{E}$ is defined by

$$\mathbf{E} \equiv \frac{1}{2}(\mathbf{F}^{\mathrm{T}}\mathbf{F} - \mathbf{1}). \tag{2}$$

The Cauchy stress at the current configuration $\mathscr{B}$ is obtained by

$$\boldsymbol{\sigma} = \frac{1}{\det(\mathbf{F})}\mathbf{F}\mathbf{S}^{\mathrm{PK2}}\mathbf{F}^{\mathrm{T}}. \tag{3}$$

The link between the deformation of a continuum and that of the underlying lattice is made through the Cauchy–Born hypothesis (Ericksen, 1984), which states that Bravais lattice vectors of the crystal, $\mathbf{b}^n$ $(n = 1, 2, 3)$, deform according to the macroscopic deformation gradient $\mathbf{F}$,

$$\mathbf{b}^n_{\mathscr{B}} = \mathbf{F}\mathbf{b}^n_{\mathscr{A}}. \tag{4}$$

In monatomic crystals like FCC and BCC simple metals, there are no internal degrees of freedom, and the separation $\mathbf{r}$ between any two atoms also transforms as

$$\mathbf{r}_{\mathscr{B}} = \mathbf{F}\mathbf{r}_{\mathscr{A}}. \tag{5}$$

When the deformations of the continuum and the lattice are linked via the Cauchy–Born hypothesis, the continuum strain energy density can be calculated from the interatomic potential energy of underlying lattice. Here, we have assumed temperature

$T = 0$, so there is no thermal fluctuation. As all atoms are identical, we may consider the energy of one atom at the origin to be representative. Within the framework of the embedded-atom method (Daw and Baskes, 1983), the energy per atom $\hat{\Psi}$ is

$$\hat{\Psi} = \frac{1}{2}\sum_i V(|\mathbf{r}^i|) + U(\rho), \tag{6}$$

where V is the pair potential, ρ is the ambient electron density for the atom at the origin and U is the energy required to embed this atom into this electron density. In Eq. (6), $|\mathbf{r}^i|$ is the interatomic distance and the index i runs over all atoms within a specified cut-off radius R_{cut}. Since each atom occupies a volume of a primitive unit cell, the strain energy density Ψ is related to the energy per atom $\hat{\Psi}$ by $\Psi = \hat{\Psi}/\Omega_{\mathscr{A}}$, where $\Omega_{\mathscr{A}}$ is the volume of the stress-free primitive unit cell. Given Ψ, Cauchy stress $\boldsymbol{\sigma}$ at the current configuration $\mathscr{B}$ can be obtained by substituting Eq. (6) into Eq. (3),

$$\boldsymbol{\sigma} = \frac{1}{\Omega_{\mathscr{B}}}\sum_i \left[\frac{1}{2}\frac{\partial V}{\partial r} + \frac{\partial U}{\partial \rho}\frac{\partial \rho}{\partial r}\right]\frac{\mathbf{r}^i_{\mathscr{B}} \otimes \mathbf{r}^i_{\mathscr{B}}}{|\mathbf{r}^i_{\mathscr{B}}|}, \tag{7}$$

where $\Omega_{\mathscr{B}}$ is the volume of the current primitive unit cell, and all derivatives in Eq. (7) are evaluated at $\mathbf{r}^i_{\mathscr{B}}$.

Next, the atomistic expression for the tangent modulus is introduced. Consider a further deformation from the current configuration $\mathscr{B}$ to a new configuration $\mathscr{C}$. A line element $\mathrm{d}\mathbf{x}_{\mathscr{B}}$ in configuration $\mathscr{B}$ is deformed into a line element $\mathrm{d}\mathbf{x}_{\mathscr{C}}$ in configuration $\mathscr{C}$ by the deformation gradient $\mathbf{F}^* \equiv \partial \mathbf{x}_{\mathscr{C}}/\partial \mathbf{x}_{\mathscr{B}}$. The second Piola–Kirchhoff stress with reference to configuration $\mathscr{B}$ is given by $\mathbf{S}^{*\mathrm{PK2}} \equiv \partial \Psi^*/\partial \mathbf{E}^*$, where Ψ^* is the strain energy per unit volume with reference to $\mathscr{B}$ and the Green strain $\mathbf{E}^* \equiv \frac{1}{2}(\mathbf{F}^{*\mathrm{T}}\mathbf{F}^* - \mathbf{1})$. The energy density Ψ^* is obtained from the energy per atom $\hat{\Psi}$ by $\Psi^* = \hat{\Psi}/\Omega_{\mathscr{B}}$. The rate of $\mathbf{S}^{*\mathrm{PK2}}$ is related to the rate of Green strain $\mathbf{E}^*$ by

$$\dot{\mathbf{S}}^{*\mathrm{PK2}} = \mathbf{C}^*\dot{\mathbf{E}}^*, \tag{8}$$

where $\mathbf{C}^*$, which is a function of $\mathbf{E}^*$, is defined as

$$\mathbf{C}^* \equiv \frac{\partial^2 \Psi^*}{\partial \mathbf{E}^* \partial \mathbf{E}^*}. \tag{9}$$

The tangent modulus $\mathbf{C}$ is $\mathbf{C}^*$ evaluated at $\mathbf{E}^* = \mathbf{0}$,

$$\mathbf{C} \equiv \left.\frac{\partial^2 \Psi^*}{\partial \mathbf{E}^* \partial \mathbf{E}^*}\right|_{\mathbf{E}^*=\mathbf{0}} \tag{10}$$

$$= \frac{1}{\Omega_{\mathscr{B}}}\left\{\sum_i \left[\frac{1}{2}\left(\frac{\partial^2 V}{\partial r^2} - \frac{1}{|\mathbf{r}^i_{\mathscr{B}}|}\frac{\partial V}{\partial r}\right) + \frac{\partial U}{\partial \rho}\left(\frac{\partial^2 \rho}{\partial r^2} - \frac{1}{|\mathbf{r}^i_{\mathscr{B}}|}\frac{\partial \rho}{\partial r}\right)\right]\right.$$

$$\left. \times \frac{\mathbf{r}^i_{\mathscr{B}} \otimes \mathbf{r}^i_{\mathscr{B}} \otimes \mathbf{r}^i_{\mathscr{B}} \otimes \mathbf{r}^i_{\mathscr{B}}}{|\mathbf{r}^i_{\mathscr{B}}|^2} + \frac{\partial^2 U}{\partial \rho^2}\left(\sum_i \frac{\partial \rho}{\partial r}\frac{\mathbf{r}^i_{\mathscr{B}} \otimes \mathbf{r}^i_{\mathscr{B}}}{|\mathbf{r}^i_{\mathscr{B}}|}\right)\left(\sum_i \frac{\partial \rho}{\partial r}\frac{\mathbf{r}^i_{\mathscr{B}} \otimes \mathbf{r}^i_{\mathscr{B}}}{|\mathbf{r}^i_{\mathscr{B}}|}\right)\right\}. \tag{11}$$

In the above expression, all derivatives are evaluated at $\mathbf{r}^i_{\mathscr{B}}$.

The interatomic potential-based constitutive model described above is implemented in the finite element program ABAQUS/Explicit (2001) by writing a "user material" subroutine. In the dynamic, explicit computational procedures of this package, the nonlinear response is obtained incrementally, given the internal forces created by the stresses in the elements, as well as the applied external forces at the start of an increment, time t. Finite element procedures solve for the acceleration at the start of the increment by solving the discretized local equations of motion. The velocities at time $t + \Delta t/2$ and the displacements at time $t + \Delta t$ are updated by a central difference time-integration procedure. The deformation gradient for each integration point at time $t + \Delta t$ is then calculated based on the updated displacement field. Given the calculated deformation gradient, a constitutive equation subroutine is required in order to calculate the stress in the element at time $t + \Delta t$. In the implementation of stress calculation according to the Cauchy–Born hypothesis, each material point is represented by an FCC lattice, always larger than a sphere of radius R_{cut}, which deforms according to the local continuum deformation gradient. That is, at the beginning of the calculation ($t = 0$), a set of neighboring atoms is created to represent the atomic environment. The lattice spacing is chosen such that the corresponding stress is zero. For each time increment, those neighboring atoms update their positions according to the local deformation gradient $\mathbf{F}$, which is generated according to the imposed boundary conditions. Then Cauchy stress $\boldsymbol{\sigma}$ and tangent modulus $\mathbf{C}$ are calculated by substituting the deformed positions of neighboring atoms into Eqs. (7) and (11), respectively. Thus, material properties depend exclusively on the atomistic description of the system. The efficiency of finite element calculations allows for the simulation of systems which are large compared to those achievable via molecular dynamics calculations, while the computation remains faithful to atomistic interactions at large strains. As such, this method qualifies as a multiscale approach. In the present study, the quasi-static simulations of nanoindentation are made via the dynamic, explicit procedure at low loading rates. The explicit solution method has proven to be effective in solving quasi-static problems, and is particularly efficient for large, three-dimensional simulations dominated by contact.

2.2. *Instability criterion for predicting defect nucleation*

The homogeneous nucleation of dislocations results from catastrophic elastic instability, as formulated at the continuum level by Hill (1962, 1975). Hill showed that the loss of strong ellipticity of the strain energy density function is an indication of elastic instability of a solid, because at this point discontinuous modes of deformation become admissible solutions to the equilibrium equations. Rice (1976) derived the same localization condition by admitting an incremental displacement jump across the discontinuous interface. The localized deformation manifests itself along this interface as slip or shear bands in inelastic materials. Here, we summarize the main results based on Rice's derivation and then connect these concepts to the non-linear elastic model that incorporates an appropriate interatomic potential. In the atomistic limit, the shear band represents unit shear, or a single dislocation characterized by its slip plane and slip direction.

The instability criterion given in this section can be applied in both FEM and MD simulations. Since MD simulations do not store information on the starting configuration and deformation history, it will be preferable to derive the localization condition with reference to the current configuration $\mathscr{B}$. To this end, we first consider a further deformation from the current configuration $\mathscr{B}$ to a new configuration $\mathscr{C}$ and derive the instability criterion at configuration $\mathscr{C}$. Then, we take configuration $\mathscr{C}$ to be coincident momentarily with configuration $\mathscr{B}$ and obtain the instability criterion at the current configuration. The resulting expression will be suitable for both FEM and MD implementations. Rice (1976) assumed the following rate relation to describe the material response,

$$\dot{\mathbf{S}}^* = \mathbf{L}\dot{\mathbf{F}}^{*\mathrm{T}}, \tag{12}$$

where $\mathbf{L}$ is the modulus tensor and the nominal stress tensor $\mathbf{S}^*$ is defined so that $\mathbf{nS}^*$ is the force acting, per unit area in the configuration $\mathscr{B}$, on a surface element of normal vector $\mathbf{n}$ in $\mathscr{B}$. It is related to the second Piola–Kirchhoff stress $\mathbf{S}^{*\mathrm{PK2}}$, which is defined with reference to $\mathscr{B}$, by $\mathbf{S}^* = \mathbf{S}^{*\mathrm{PK2}}\mathbf{F}^{*\mathrm{T}}$. The localization condition is determined by examining whether a bifurcation within a band of orientation $\mathbf{n}$ is possible such that the continuing kinematical and equilibrium conditions are satisfied. To maintain continuous velocity across the imaginary interface between stable and unstable regions, the change in deformation gradient $\dot{\mathbf{F}}^*$ across the discontinuous surface must be of the form,

$$\Delta\dot{\mathbf{F}}^* = \mathbf{g} \otimes \mathbf{n}, \tag{13}$$

where $\mathbf{g}$ is the relative displacement vector across the interface. The continuous equilibrium condition requires that the difference of $\dot{\mathbf{S}}^*$ across the discontinuous surface satisfies,

$$\mathbf{n}\Delta\dot{\mathbf{S}}^* = 0. \tag{14}$$

Then, substitution of the constitutive law defined by Eq. (12) and the continuing kinematical condition given by Eq. (13) into the equilibrium condition Eq. (14) gives,

$$(\mathbf{nLn})\mathbf{g} = 0. \tag{15}$$

The onset of localization occurs when a non-trivial solution of $\mathbf{g}$ exists. That is, the acoustical tensor $\mathbf{Q}(\mathbf{n}) \equiv \mathbf{nLn}$ becomes singular (Rice, 1976),

$$\det[\mathbf{Q}(\mathbf{n})] = 0. \tag{16}$$

From energy analysis, it can be proven that the acoustical tensor $\mathbf{Q}(\mathbf{n})$ is positive definite when the material is stable, e.g., Rice (1976). Therefore, the determinant function $\det[\mathbf{Q}(\mathbf{n})]$ will approach zero from the positive side. The dislocation will be homogeneously nucleated when the determinant function $\det[\mathbf{Q}(\mathbf{n})]$ attains zero-value for the first time. The associated eigenvector $\mathbf{g}$ calculated from the matrix of $\mathbf{Q}(\mathbf{n})$ will represent the slip vector at the onset of dislocation nucleation.

The instability condition based on the above bifurcation analysis will be applied to the current configuration $\mathscr{B}$ to detect dislocation nucleation once Cauchy stress $\boldsymbol{\sigma}$ and tangent modulus $\mathbf{C}$ are calculated through either FEM or MD simulations. To study bifurcation in configuration $\mathscr{B}$, we take configuration $\mathscr{C}$ to be coincident momentarily

with configuration $\mathscr{B}$, i.e., $\mathbf{F}^* = \mathbf{1}$. Under this condition, the following relations can be easily derived,

$$\dot{\mathbf{S}}^* = \dot{\mathbf{S}}^{*\mathrm{PK2}} + \boldsymbol{\sigma}\dot{\mathbf{F}}^{*\mathrm{T}}, \tag{17}$$

$$\dot{\mathbf{E}}^* = \frac{1}{2}(\dot{\mathbf{F}}^* + \dot{\mathbf{F}}^{*\mathrm{T}}). \tag{18}$$

Substituting Eqs. (17) and (18) into Eq. (12), and using Eq. (8), one obtains,

$$L_{ijkl} = C_{ijkl} + \sigma_{il}\delta_{jk}. \tag{19}$$

Cauchy stress $\boldsymbol{\sigma}$ in configuration $\mathscr{B}$ arises in the expression of the modulus tensor $\mathbf{L}$ because the current configuration $\mathscr{B}$ is generally a stressed state. Since the modulus tensor $\mathbf{L}$ is calculated according to the atomistically informed Cauchy stress $\boldsymbol{\sigma}$ and tangent modulus $\mathbf{C}$ in configuration $\mathscr{B}$, as defined by Eqs. (7) and (11), the crystal lattice information is incorporated automatically. This tensor has the symmetry

$$L_{ijkl} = L_{lkji}, \tag{20}$$

but,

$$L_{ijkl} \neq L_{jikl}, \quad L_{ijkl} \neq L_{ijlk}, \tag{21}$$

as $\mathbf{g}$ and $\mathbf{n}$ are conceptually distinct vectors. Thus, Eq. (16) fully defines the site and slip character of dislocations nucleated within simulations of calculable $\boldsymbol{\sigma}$ and $\mathbf{C}$.

Homogeneous nucleation of a defect has been studied in the context of elastic wave instability by Li et al. (2002). That is, the defect nucleation is realized by a dynamic process which comprises the progressive steepening of a localized wave front and arrest of the final atomistically sharp wave front in a low-dimensional atomic energy landscape. The free energy-based Λ-criterion for wave instability (Li et al., 2002) is equivalent to the defect nucleation criterion given by Eq. (16). The wavevector $\mathbf{k}$ and the polarization vector $\mathbf{w}$ for the unstable transverse wave corresponds to the slip plane normal $\mathbf{n}$ and the associated slip vector $\mathbf{g}$, respectively. Though the current study is not concerned with dynamics, the defect nucleation criterion given by Eq. (16) is still referred to as the Λ-criterion.

2.3. Calibration of EAM potentials by ab initio calculation

Recent advances in optimal parametrization of the interatomic potential (Mishin et al., 1999, 2001) enable improved accuracy of the constitutive model of interatomic potential-based hyperelasticity, within its intrinsic limitations. The EAM potential for Cu (Mishin et al., 2001) is employed in the present indentation simulations. The elastic constants (at the stress-free state) and stacking fault energies obtained from experiments and calculated via the EAM-Mishin potential are given in Table 1. For comparison, the corresponding values calculated from another commonly used EAM potential by Ackland et al. (1997) are also listed in Table 1.

Table 1
Elastic constants and intrinsic stacking fault energies for Cu

Method	C_{11} (GPa)	C_{12} (GPa)	C_{44} (GPa)	γ_{sf} (mJ/m^2)
Experiment	168.4	121.4	75.4	45
EAM-Mishin	169.9	122.6	76.2	44.4
EAM-Ackland	168.4	121.3	75.3	46.8

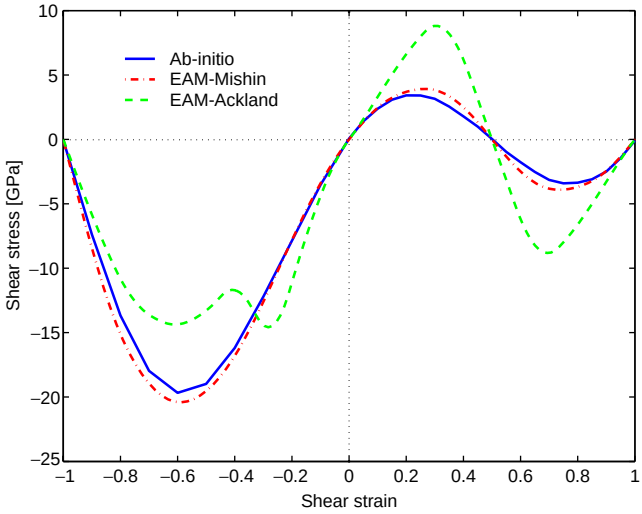

Fig. 1. Stress versus strain curves for simple shear of Cu.

A reliable potential should not only fit well the single point properties such as elastic constants and the intrinsic stacking fault energy, but also characterize accurately the deformation path up to the elastic limit. Consider a homogeneous simple shear deformation on the $(1\,1\,1)$ plane along the $[1\,1\,\bar{2}]$ direction. The dash-dot line in Fig. 1 shows the shear stress versus shear strain response predicted by the EAM-Mishin potential. Here, the shear strain is defined by the shear displacement divided by the Shockley partial slip in the $[1\,1\,\bar{2}]$ direction $a_0/\sqrt{6}$, where a_0 is the lattice constant. In order to test the accuracy of the EAM-Mishin potential, an ab initio DFT calculation is performed whereby simple shear deformation is applied to a six-atom supercell of three $\{1\,1\,1\}$ layers. The stress versus strain response in the DFT calculation is obtained by using the generalized gradient approximation (GGA) within an ultrasoft pseudopotential total energy scheme (Ogata et al., 2002). It can be seen from Fig. 1 that the prediction via the EAM-Mishin potential is in good agreement with the ab initio calculation. Fig. 1 also shows the shear stress versus strain curve based on the EAM-Ackland potential. Compared with the ab initio DFT calculation, the EAM-Mishin potential gives

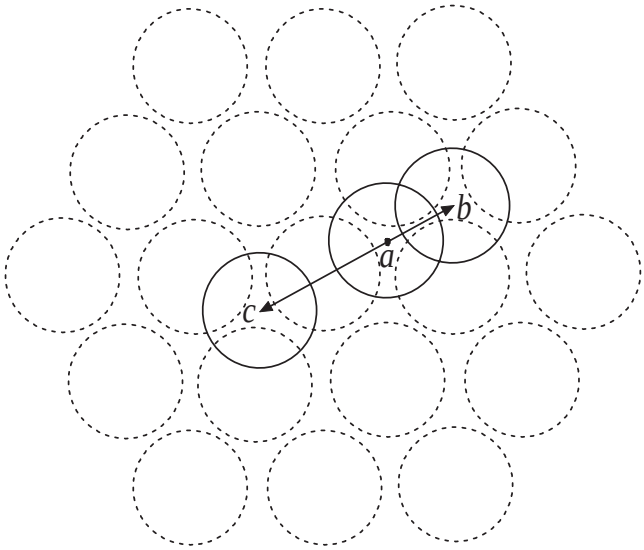

Fig. 2. Schematics of shear along the Shockley partial slip $[1\,1\,\bar{2}]$ direction (from site a to b) and reversed shear along the $[\bar{1}\,\bar{1}\,2]$ direction (from site a to c) above the close-packed $(1\,1\,1)$ plane.

a more accurate description of finite shear deformation than does the EAM-Ackland potential. We demonstrate below that the choice of a reliable potential is critical for an accurate prediction of both the load versus displacement response and mode of dislocation nucleation in nanoindentation simulations.

The above simple shear calculations also reveal an important feature at finite deformation, i.e., asymmetry of shear stress response with respect to the shear direction. It can be seen from Fig. 1 that the critical shear stress in the $[1\,1\,\bar{2}]$ direction (3.91 GPa) is much lower than the peak stress when sheared in the opposite direction, i.e., the $[\bar{1}\,\bar{1}\,2]$ direction (20.4 GPa). This asymmetry in critical shear stress is due to the effect of finite deformation, and can be understood by examining the relative motion between adjacent close-packed planes in an FCC crystal. In Fig. 2, the dashed circles represent one atomic layer of the close-packed $(1\,1\,1)$ plane. The solid circles represent atoms above this layer, and are originally located in sites such as the one denoted by a. The shear along the partial slip $[1\,1\,\bar{2}]$ direction corresponds to motion of the atom from site a to b and the reversed shear along the $[\bar{1}\,\bar{1}\,2]$ direction from site a to c. It is immediately evident from Fig. 2 that, within the finite shear deformation regime, the reversed shear along the $[\bar{1}\,\bar{1}\,2]$ direction requires a larger dilatation normal to the slip plane due to the misfit of adjacent plane atoms, and hence needs to overcome a larger energy barrier. Consequently, the critical shear stress in the $[\bar{1}\,\bar{1}\,2]$ direction will be much higher relative to that in the $[1\,1\,\bar{2}]$ direction. Therefore, not only the magnitude of shear stress but also the direction and the sense of shear deformation are relevant in defining and predicting dislocation nucleation. This dependence of the homogeneous dislocation nucleation barrier on shear direction is in contrast to the conventional

crystal plasticity model which assumes the symmetric resistance for the motion of existing dislocations (Asaro, 1983). The assumption of a symmetric slip barrier is based on the statistical nature of the resistances which include forest dislocations threading through the slip plane, solute atoms or second phase particles acting as discrete obstacles in the slip plane.

3. Indentation on a linear anisotropic elastic solid

As a complementary analysis of nanoindentation via interatomic potential-based hyperelasticity, the analytic solutions for frictionless indentation on a linear elastic, single crystal are given in this section for both 2D and 3D configurations. Analytic insights regarding the effects of crystalline anisotropy are discussed, and serve to rationalize the results of interatomic potential-based finite element simulations.

3.1. 2D indentation by a cylindrical indenter

Consider a frictionless cylindrical indenter of radius R pressed into a linear anisotropic elastic half-space, as shown in Fig. 3. The coordinate system is oriented such that the x_3 axis is parallel to the axial direction of the cylinder. Within the regime of linear elastic deformation, the resulting displacement field is only a function of in-plane coordinates (x_1, x_2) and has no variation in the out-of-plane x_3 direction. This is a generalized two-dimensional problem which can be solved by recourse to the Stroh formalism given in Appendix A. Fan and Hwu (1996) derived the general solution of punch indentation on a linear anisotropic elastic half-space. We apply this general solution to the present geometric configuration. To first order, the cylindrical profile can be approximated by a parabola. By solving a standard Hilbert problem, the derivative

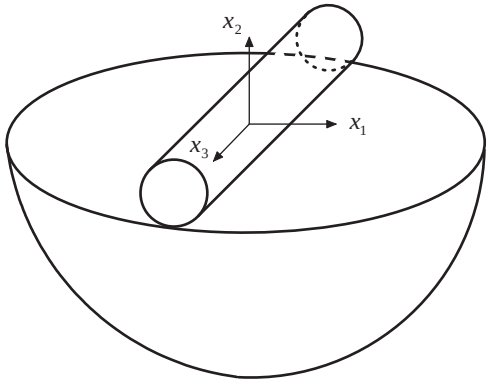

Fig. 3. Schematics of 2D indentation: a cylindrical indenter on an elastic half-space.

of the complex function $\mathbf{f}$, as defined in Appendix A, is given by

$$\mathbf{f}' = \frac{i}{2(\mathbf{M}^{-1})_{22}R}\begin{bmatrix} (\mathbf{B}^{-1})_{12}\left(z_1 - \sqrt{z_1^2 - a^2}\right) \\ (\mathbf{B}^{-1})_{22}\left(z_2 - \sqrt{z_2^2 - a^2}\right) \\ (\mathbf{B}^{-1})_{32}\left(z_3 - \sqrt{z_3^2 - a^2}\right) \end{bmatrix}, \tag{22}$$

where $i = \sqrt{-1}$, a denotes contact half-width, and the matrices $\mathbf{B}$ and $\mathbf{M}$, as defined in Appendix A, can be determined uniquely for a given set of the material elastic constants. The subscript in Eq. (22) denotes the corresponding component of the matrix. The stress field is obtained by substituting the above expression into Eqs. (A.12) and (A.13). Note that a difficulty arises in deriving the 2D load-penetration relation which is absent in the 3D case: For an elastic half-space loaded two-dimensionally, the displacement field decays logarithmically from the contact point (Johnson, 1985). Thus, there exist arbitrary, unresolved constants for the displacement field such that the load-penetration relation depends on the system size and the boundary conditions. However, the analytic expression relating indentation load and contact half-width can be obtained by requiring that the stress singularity at the contact edge vanishes. This explicit relation is given by

$$P = \frac{\pi a^2}{2(\mathbf{M}^{-1})_{22}R}. \tag{23}$$

The corresponding solution for isotropic elasticity has the same functional form, except that the value $(\mathbf{M}^{-1})_{22}$ is replaced by $(1-\nu)/\mu$, where μ is shear modulus and ν is Poisson's ratio.

Based on the complex function given by Eq. (22), the stress distribution beneath the indenter is calculated for a cylindrical indentation normal to the (1 1 1) surface of Cu along the $[1\,\bar{1}\,0]$ direction. The coordinate system in Fig. 3 is oriented such that the x_1 and x_2 axes correspond with the $[1\,1\,\bar{2}]$ and [1 1 1] directions, respectively. The out-of-plane x_3 axis is along the $[1\,\bar{1}\,0]$ direction. The elastic constants for single crystal Cu are taken to be the values fitted by the Mishin potential as listed in Table 1. The radius of the indenter R is taken to be 50 Å, and the imposed contact half-width is chosen as $a = 17.4$ Å to facilitate comparison with MD and FEM simulations. The distribution of Mises stress beneath the indenter is shown in Fig. 4(a). The effect of material anisotropy is revealed by comparing the Mises stress contour for an isotropic material (Johnson, 1985) with that for single crystal Cu. For an isotropic material, this stress distribution is symmetric with respect to x_2 axis. Taking Poisson's ratio to be 0.3, the point of maximum Mises stress is along x_2 axis at a depth of $0.70a$. For single crystal Cu, the anisotropy factor, defined by $2C_{44}/(C_{11} - C_{12})$, is 3.22. As shown in Fig. 4(a), the Mises stress contour is not symmetric about x_2 axis due to this elastic anisotropy. The point of maximum Mises stress is off-center by $0.24a$ and at a depth of $0.66a$. The corresponding maximum Mises stress is 10.16 GPa.

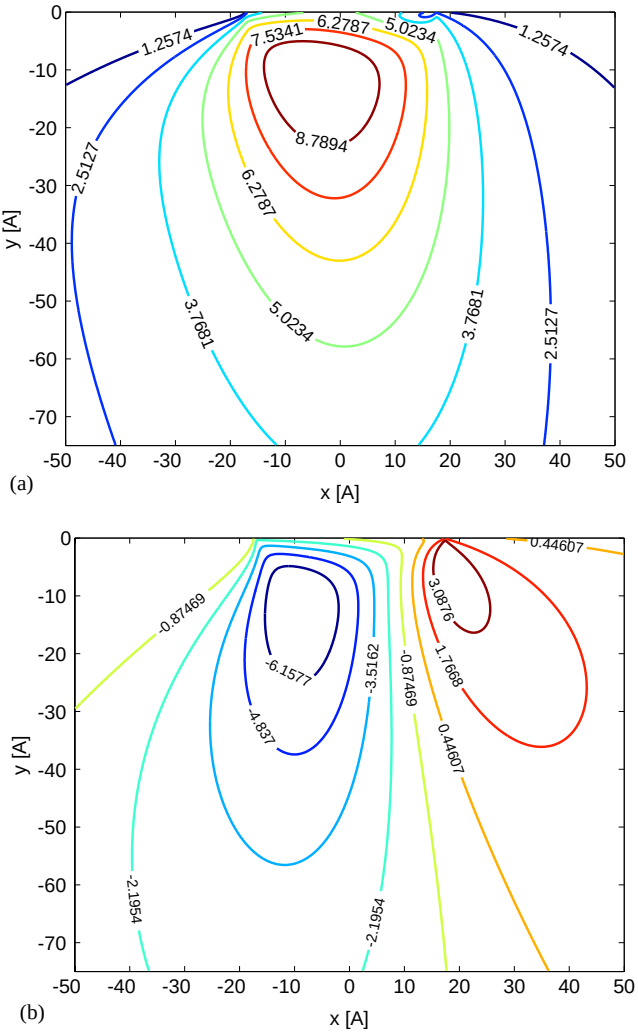

Fig. 4. Stress contour beneath a cylindrical indenter from the 2D analytic solution: (a) Mises stress, (b) Shear stress resolved into $(1\,1\,\bar{1})[1\,1\,2]$ slip system. The numbers indicated on the contour map are in units of GPa.

Dislocations tend to nucleate and move on certain close-packed slip planes and directions in crystalline metals. The shear stresses resolved into the FCC primary slip systems of $\{1\,1\,1\}\langle 1\,\bar{1}\,0\rangle$ and $\{1\,1\,1\}\langle 1\,1\bar{2}\rangle$ are calculated. For the current orientation of the underlying crystal structure with respect to the indentation loading axis, the maximum magnitude of resolved shear stress is on the Shockley partial slip system $(1\,1\,\bar{1})[1\,1\,2]$. The slip plane $(1\,1\,\bar{1})$ is oriented at 19.47° with respect to x_2 axis. Fig. 4(b) shows the contour of resolved shear stress on the $(1\,1\,\bar{1})[1\,1\,2]$ slip system.

The point of maximum magnitude of resolved shear stress lies to the left of x_2 axis by $0.54a$ and at a depth of $0.66a$. The corresponding resolved shear stress is -7.55 GPa.

Analytic insights gained from the above linear elastic analysis can be used to rationalize numerical simulations. First, for this particular orientation, the out-of-plane displacement is null due to the mirror symmetry of the lattice with respect to the $(1\,\bar{1}\,0)$ plane (prior to the possible symmetry breaking caused by the elastic instability). Therefore, this is a true plane strain problem within the elastic deformation regime. No further approximation is needed for this generalized plane strain problem when using plane strain elements in 2D finite element simulations. More importantly, the choice of the current indenter geometry will facilitate the study of homogeneous nucleation of dislocation in the bulk by mitigating surface effects. That is, for the current orientation, the resolved shear stress reaches its maximum value at some distance beneath the surface. This is in contrast with the computational nanoindentation study by Tadmor et al. (1999a), which examined the same crystallographic orientation as considered in the present work, but under a rectangular punch indenter. The sharp corners of such an indenter induce dislocation emission from the contact point at the surface, where the interpretation of atomic stress at free surfaces is unclear (Cheung and Yip, 1991) and the role of ledge formation is difficult to quantify unambiguously.

3.2. 3D indentation by a spherical indenter

The analytic load versus displacement relation is given in this subsection for indentation of a spherical indenter on the $\{1\,1\,1\}$ surface of a single crystal half-space. Fig. 5 shows a spherical indenter of radius R in contact with a linear elastic anisotropic half-space. The coordinate system is oriented such that x_1, x_2 and x_3 axes correspond with the $[1\,1\,\bar{2}]$, $[1\,1\,1]$ and $[1\,1\,0]$ directions, respectively. To first order, the spherical indenter can be approximated by a paraboloid. The general elastic solution for the indentation on an anisotropic half-space by a paraboloid was first derived by Willis (1966) using the Fourier transform technique. Based on the Green's function for an elastic, anisotropic half-space (Barnett and Lothe, 1975), the simplified elastic

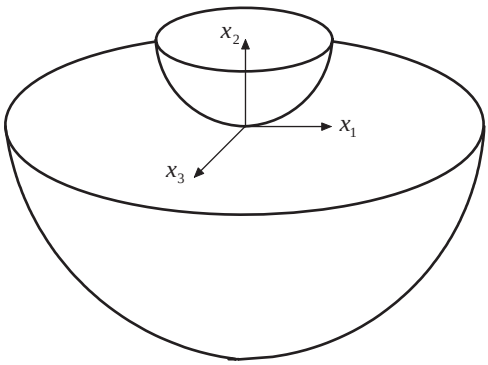

Fig. 5. Schematics of 3D indentation: a spherical indenter on an elastic half-space.

solutions for the indentation load versus displacement response were given by Vlassak and Nix (1993, 1994), Swadener and Pharr (2001) for various indenter profiles. Willis (1966) showed that the contact area produced by a paraboloid on an anisotropic, elastic half-space is elliptical in shape. For indentation normal to a $\{1\,1\,1\}$ surface with inherent three-fold rotational symmetry, the contact area is circular. The load P versus penetration h relation is simply given by

$$P = \frac{4}{3} E^* R^{1/2} h^{3/2}, \tag{24}$$

where the indentation modulus E^* is

$$E^* = \left(\frac{1}{4\pi} \int_0^{2\pi} \hat{\mathbf{L}}_{22}^{-1}(\gamma)\, \mathrm{d}\gamma \right)^{-1}. \tag{25}$$

In Eq. (25), the Barnett–Lothe tensor $\hat{\mathbf{L}}$, defined by Eq. (A.14) in Appendix A, is calculated in the transformed x_1'–x_2–x_3' coordinate system, which is obtained by rotating x_1 and x_3 axes in the x_1–x_3 plane an angle γ about x_2 axis. For an isotropic material deformed via a rigid indenter, the indentation modulus E^* reduces to $E/(1-\nu^2)$, where E denotes Young's modulus. The above analytic solution will be used to benchmark 3D FEM simulations. For elastic constants fitted by the EAM-Mishin potential as given in Table 1, the value of E^* calculated from Eq. (25) is 153 GPa.

4. 2D nanoindentation-induced dislocation nucleation

4.1. Validation of FEM simulations

In this section, FEM simulations using interatomic potential-based hyperelasticity is validated by comparing 2D cylindrical indentation results with direct MD simulations. The same interatomic potential of Cu fitted by Mishin et al. (2001) is used for the constitutive input of FEM simulations and MD interatomic force field calculations. The indentation orientation is the same as that for the linear analysis in Section 3. That is, a cylindrical indenter along the $[1\,\bar{1}\,0]$ direction is imposed normal to the $(1\,1\,1)$ surface.

ABAQUS/Explicit (2001) is implemented to simulate 2D indentation. A small system size, 200×100 Å, is simulated for direct comparison with MD calculations. Plane strain linear, triangular elements are used, with each element representing a homogeneously deformed crystallite. The boundary conditions are fixed at the bottom, free on the top surface and fixed in the x_1 directions on two sides. The cylindrical indenter is defined by an analytic rigid surface with a radius R of 50 Å. The contact between the indenter and the surface is frictionless. The quasi-static solution is approximated by maintaining the kinetic energy at less than 1% of the internal energy of the system.

MD simulations at the temperature 1 K are performed to compare with FEM calculations. The same in-plane boundary conditions as FEM simulations are used and periodic boundary conditions (PBC) are applied for the out-of-plane x_3 direction. In order to follow the minimum image convention in MD implementation, ten layers of

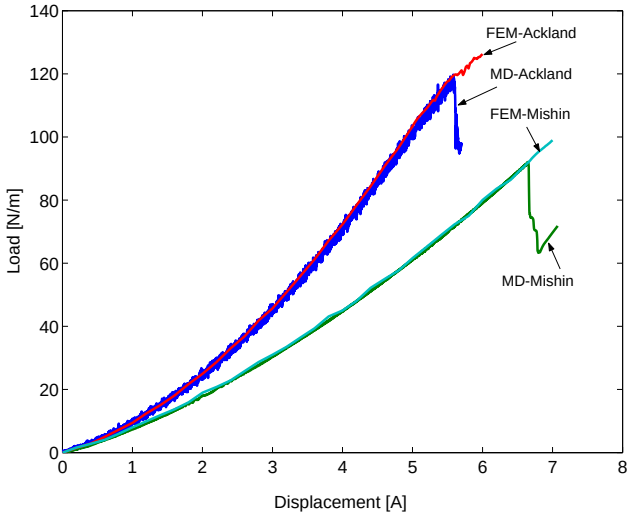

Fig. 6. Load versus displacement curves of nanoindentation by a cylindrical indenter from FEM and MD simulations.

atoms are used along the x_3 direction. This ensures that the half-thickness of the PBC box is greater than the Mishin potential cut-off radius. The indenter is regarded as an external repulsive potential interacting with copper atoms at the surface (Kelchner et al., 1998),

$$\Psi^{\text{ext}}(r) = AH(R-r)(R-r)^3, \tag{26}$$

where A is a force constant and $H(r)$ is the step function. In the present calculations, $A = 10$ eV/Å^3. The indentation proceeds in displacement-control at a speed of about 1 m/s.

The calculated nanoindentation responses based on the Mishin potential are given in Fig. 6. It can be seen that the P–h responses predicted by FEM and MD are in good agreement. The MD response shows a sharp drop in load at an indentation depth of 6.65 Å, which indicates the onset of homogeneous nucleation of dislocation within the crystal. This load drop was not captured in the corresponding FEM simulation because the 2D setting constrains the out-of-plane displacement mode that the homogeneously nucleated dislocation takes, as shown in the MD simulation. Fig. 6 also shows the P–h response calculated via the Ackland potential for the same indenter radius and crystallographic orientation. Though agreement between FEM and MD predictions based on the Ackland potential further validates the FEM calculation, the significant differences in the predicted P–h response and critical load drop point given by each of these potentials underscore the importance of optimal parametrization of the interatomic potential.

The calculated stress distribution beneath the indenter is compared between FEM and MD simulations based on the Mishin potential. FEM stress computation at each material point follows the constitutive model of interatomic potential-based hyperelasticity as given by Eq. (7), which is dictated by the local deformation gradient. In contrast,

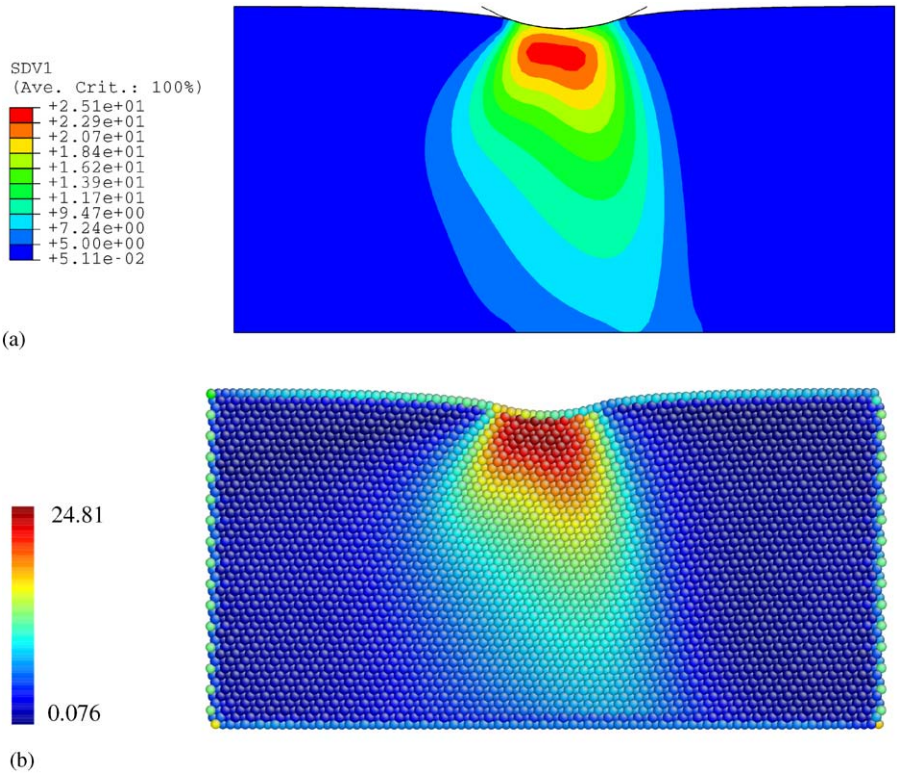

Fig. 7. Contours of Mises stress (in GPa) beneath a cylindrical indenter: (a) FEM and (b) MD simulations.

for every atom in the MD simulation, atomic Cauchy stresses are calculated by substituting the actual coordinates of neighboring atoms into Eq. (7). Thus the positions of neighboring atoms are explicitly tracked for every time step. Though the definition of atomic Cauchy stress is not strictly well-posed in terms of the continuum concept of stress, the value of atomic stress represents an effective measure of the stress state imposed on each atom. Figs. 7(a) and (b) show the contours of Mises stress calculated from FEM and MD simulations, respectively. The indentation depth is 6.65 Å, corresponding to the indenter displacement immediately preceding dislocation nucleation. It can be seen that the FEM prediction based on interatomic potential-based hyperelasticity is in good agreement with that of the MD simulation. Both simulations give the maximum Mises stress about 25 GPa. However, the Mises stress contours shown in Figs. 7(a) and (b) differ significantly from the linear elastic result for indentation on a 2D half-space, as shown in Fig. 4(a) for the same contact half-width as FEM/MD simulations. These differences can be attributed to the elastic nonlinearity of the highly deformed material near the indenter and the boundary effects due to the finite size of the simulated system.

4.2. MD simulation of dislocation nucleation

Though MD simulations are limited by the achievable length and time scales, this approach has the distinct advantage of allowing defects to nucleate and evolve spontaneously, without prescribing the site and nature of such defects. Thus, the atomic structure of the emerging dislocation is directly revealed by MD simulations. Fig. 8(a) shows the embryo of a homogeneously nucleated dislocation via MD simulation using the Mishin potential. Atoms are color-encoded by coordination number N (Li, 2003). Perfectly coordinated atoms, $N = 12$, are color-encoded as yellow, and other colored atoms indicate $N \neq 12$. Tracing of atomic trajectories indicates that relative motion between the left and right two $(1\,1\,\bar{1})$ layer blue atoms represents a Shockley partial slip along the $[1\,\bar{2}\,\bar{1}]$ direction within the $(1\,1\,\bar{1})$ slip plane. This partial slip takes a mixed in-plane and anti-plane shear mode. Due to the 2D nature of MD simulations, the homogeneously nucleated defect is a dislocation line with the $[1\,\bar{1}\,0]$ line direction perpendicular to the x_1–x_2 plane. Note that there is another equivalent Shockley partial slip direction $[\bar{2}\,1\,\bar{1}]$ due to mirror symmetry of the $(1\,1\,\bar{1})$ slip plane with respect to the x_1–x_2 plane. In a MD simulation, activation of either of these two equivalent Shockley partial slip systems is possible and dependent on numerical noise.

For comparison, Fig. 8(b) displays the atomic structure of the homogeneously nucleated dislocation via MD simulation using the Ackland potential. It can be seen that the activated slip system of the Shockley partial is on the $(1\,1\,\bar{1})$ plane and along the $[\bar{1}\,\bar{1}\,\bar{2}]$ direction. In contrast to the mixed shear mode of the Shockley partial slip predicted by the Mishin potential, the simulation via the Ackland potential generates a partial slip event with a pure in-plane shear mode. This discrepancy in slip orientation can be correlated with the simple shear calculations given in Fig. 1, which shows that the Ackland potential predicts a fictitiously high critical stress when sheared in the $[1\,1\,\bar{2}]$ direction and a decrease in critical shear stress when sheared in the reversed direction, with respect to calculations via the Mishin potential. When using the Ackland potential in nanoindentation simulation, due to this artifactual reduction of the shear barrier in the $[\bar{1}\,\bar{1}\,\bar{2}]$ direction (equivalent to the $[\bar{1}\,\bar{1}\,2]$ direction in Fig. 2), the Shockley partial slip is first developed along this direction. In contrast, the high shear barrier along the $[\bar{1}\,\bar{1}\,\bar{2}]$ direction for the Mishin potential forces the Shockley partial slip to develop in the $[1\,\bar{2}\,\bar{1}]$ direction. This slip direction is equivalent to the $[1\,1\,\bar{2}]$ direction in Fig. 2 and hence has a much lower critical stress. The MD simulations are terminated at this point because further evolution of the dislocation structure, including heterogeneous nucleation of dislocations and interaction among dislocations, depend strongly on the loading rate and the simulated system size. This topic on massive dislocation activity beneath the indenter is addressed by Van Vliet et al. (2003).

4.3. Prediction of dislocation nucleation by instability criterion

Continuum level defect nucleation studies require a reliable instability criterion which should capture the moment, location and nature of homogenously nucleated defects. Below, both the interatomic potential-based Λ-criterion and the critical resolved shear

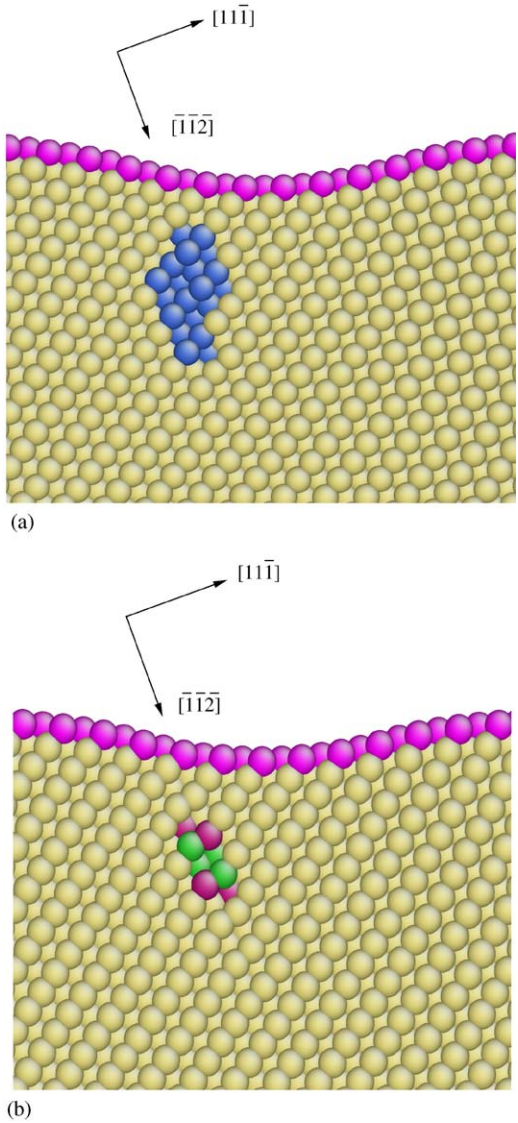

Fig. 8. MD simulations of nanoindentation by a cylindrical indenter: atomic structure of homogeneously nucleated dislocation on the $(1\,1\,\bar{1})$ plane. (a) Shockley partial slip along the $[1\,\bar{2}\,\bar{1}]$ direction from Mishin potential; (b) Shockley partial slip along the $[\bar{1}\,\bar{1}\,\bar{2}]$ direction by Ackland potential.

stress (CRSS) criterion are evaluated by comparing the corresponding defect nucleation predictions with those obtained via direct MD simulations.

Since all the atomic information is channeled through the Cauchy stress $\boldsymbol{\sigma}$ and tangent modulus $\mathbf{C}$, the Λ-criterion can be readily incorporated into finite element analysis. Localization indicator $\det[\mathbf{Q}(\mathbf{n})]$ is calculated at the element level to detect dislocation

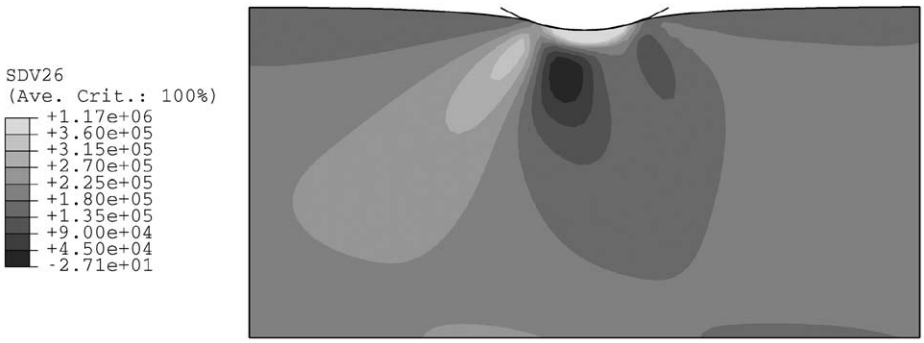

Fig. 9. Contour of det[$\mathbf{Q}(\mathbf{n})$] by 2D FEM simulation.

nucleation. Testing for the formation of a localization surface involves a search over all the possible orientations specified by the vectors $\mathbf{n}$. Given the atomistically informed $\mathbf{L}$ tensor, the general algorithm for searching critical surfaces involves a constrained 6-dimensional minimization by which the localization surface normal $\mathbf{n}$ and the direction of relative displacement vector $\mathbf{g}$, as defined in Section 2.2, are determined simultaneously (Li et al., 2002; Van Vliet et al., 2003). For the FCC lattice considered here, we simply trace the current surface normals $\mathbf{n}$ of close-packed $\{1\,1\,1\}$ slip planes from their initial surface normals $\mathbf{n^0}$ by the relation $\mathbf{n} = \mathbf{n^0}\,\mathbf{F}^{-1}$ (Asaro, 1983). When an instability occurs, the acoustical tensor $\mathbf{Q}(\mathbf{n})$ will no longer be positive definite.

Fig. 9 shows the contour of det[$\mathbf{Q}(\mathbf{n})$] at an indentation depth of 6.68 Å, corresponding to the moment when the onset of dislocation nucleation is first detected at one integration point. The critical indentation depth predicted by FEM calculation is in good agreement with that by MD simulation. In calculating det[$\mathbf{Q}(\mathbf{n})$], the modulus $\mathbf{L}$ is normalized via the elastic constant $C_{44} = 75.4$ GPa. It can be seen from Fig. 9 that the interpolated values of det[$\mathbf{Q}(\mathbf{n})$] within the dark grey region beneath the indenter are small negative values, which indicate the site of a homogeneously nucleated dislocation. The position of this dislocation nucleation site is 14.25 Å below the surface, and displaced 5.75 Å from the central x_2 axis, while the center of dislocation core in MD simulation shown in Fig. 8(a) is approximately 16.66 Å below the surface and displaced 5.16 Å from the x_2 axis. Thus, FEM prediction of the nucleation site agrees well with that of MD simulations, to one atomic lattice spacing. The direct prediction of slip directions via the eigenvector analysis of the corresponding matrix $\mathbf{Q}(\mathbf{n})$ is limited by the present, highly symmetric crystallographic orientation. MD simulations indicate that the Shockley partial slip develops along one of two equivalent slip directions, i.e., $[1\,\bar{2}\,\bar{1}]$ or $[\bar{2}\,1\,\bar{1}]$, within the $(1\,1\,\bar{1})$ plane. This is a degenerate-eigenvector situation which can be detected numerically by diagonalization of the matrix $\mathbf{Q}(\mathbf{n})$. For the degenerate case, the slip orientations resulting from the instability can be identified from crystallographic symmetry, without resorting to a higher-order (cubic, quartic) analysis of the strain energy.

For comparison, the stress-based dislocation nucleation criterion (CRSS) is also evaluated in FEM calculations using the constitutive model of interatomic potential-based

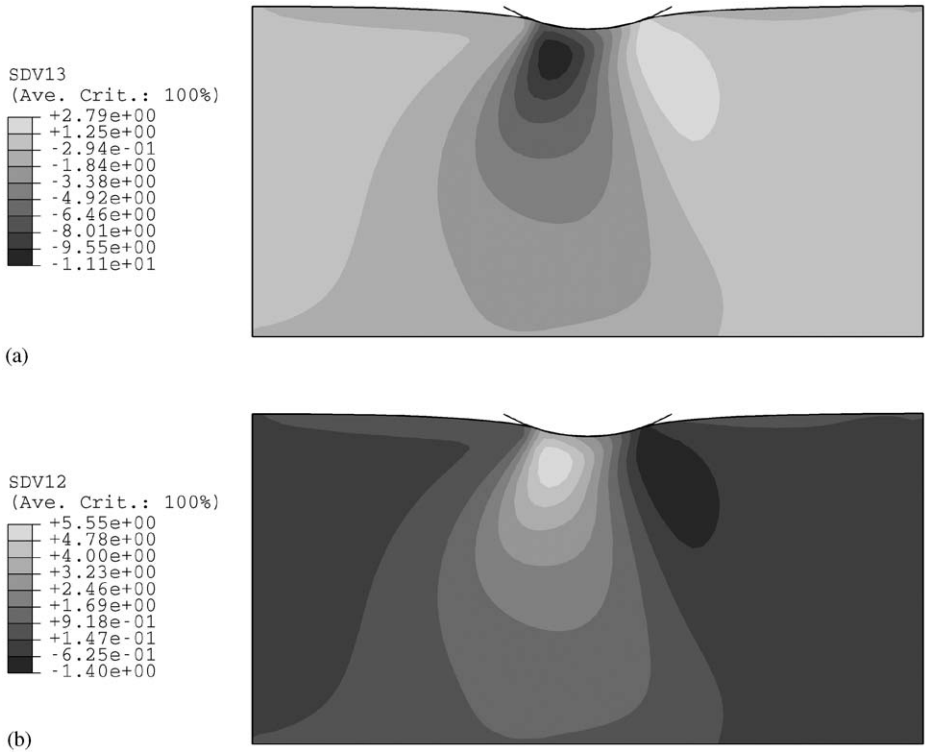

Fig. 10. Distribution of resolved shear stress (in GPa) by 2D FEM simulation: (a) $(1\,1\,\bar{1})[1\,1\,2]$ slip system, (b) $(1\,1\,\bar{1})[1\,\bar{2}\,\bar{1}]$ slip system.

hyperelasticity. The linear elastic analysis indicates that the maximum resolved shear stress occurs on the Shockley partial slip system $(1\,1\,\bar{1})[1\,1\,2]$, while the MD simulation indicates that the dislocation will nucleate in one of two other equivalent slip systems, $(1\,1\,\bar{1})[1\,\bar{2}\,\bar{1}]$ or $(1\,1\,\bar{1})[\bar{2}\,1\,\bar{1}]$. Since the critical shear stress sensitively depends on other local stress components (Ogata et al., 2002) as discussed in Introduction, the value of CRSS corresponding to the local stress environment associated with nanoindentation is a priori unknown. Therefore, we back out the value of CRSS within a nanoindentation-induced stress field from the Λ-criterion. Specifically, the shear stresses resolved into different slip systems are calculated when the indenter is displaced to the critical depth for dislocation nucleation as predicted by the Λ-criterion. Figs. 10(a) and (b) show contours of resolved shear stress on $(1\,1\,\bar{1})[1\,1\,2]$ and $(1\,1\,\bar{1})[1\,\bar{2}\,\bar{1}]$ slip systems from FEM calculations. It can be seen from Fig. 10(a) that the shear stress along the $[1\,1\,2]$ direction maximizes on the right side of the x_2 axis with a value about 2.8 GPa and the shear stress along the $[\bar{1}\,\bar{1}\,\bar{2}]$ direction maximizes on the left side with a value approximately 11.1 GPa. In contrast, Fig. 10(b) shows that the shear stress in the $[1\,\bar{2}\,\bar{1}]$ direction maximizes on the left side of the x_2 axis with a value about 5.6 GPa and the shear stress along the $[\bar{1}\,2\,1]$ direction maximizes on the right side

with a value about 1.4 GPa. Due to the asymmetric instability threshold for finite shear deformation, the dislocation will nucleate along the $[1\,\bar{2}\,\bar{1}]$ direction as shown in MD simulations, though the magnitude of the corresponding resolved shear stress, 5.6 GPa, is smaller than that in the $[\bar{1}\,\bar{1}\,\bar{2}]$ direction, 11.1 GPa. Thus the critical shear stress for nanoindentation by a cylindrical indenter is determined to be 5.6 GPa. This value is much higher than that for the unrelaxed simple shear (3.4 GPa) from DFT calculation since the instability occurs within a highly compressive stress environment associated with nanoindentation. This result reinforces the concept that the critical shear stress required to nucleate a dislocation homogeneously is not a unique value, but is in fact quite dependent on the local stress state of the crystal.

The site of maximum resolved shear stress along the $[1\,\bar{2}\,\bar{1}]$ direction shown in Fig. 10(b) is about 9.9 Å below the surface and 9.2 Å on the left of x_2 axis. It differs from the site of minimum $\det[\mathbf{Q}(\mathbf{n})]$ shown in Fig. 9. MD simulation of the dislocation nucleation process verifies that the Λ-criterion accurately predicts the location of dislocation nucleation, whereas the CRSS criterion is only approximate. The advantages of the Λ-criterion over the CRSS criterion could be further appreciated as follows: The Λ-criterion is parameter-free for a given lattice structure and interatomic potential. Dislocation nucleation occurs as a natural consequence of losing the positive-definite property of the acoustical tensor $\mathbf{Q}(\mathbf{n})$. Moreover, the influence of the stress state on instability is embedded in the $\mathbf{L}$ tensor. For the CRSS criterion, the threshold needs to be calibrated and a fixed value of CRSS is unable to capture accurately instability for various stress states.

5. 3D nanoindentation-induced dislocation nucleation

In this section, we present 3D simulations of nanoindentation by a spherical indenter to quantify the critical state of dislocation nucleation in single crystal Cu. Actual experimental conditions are approached by creating a system size larger than that attainable via atomistic simulations and by maintaining a quasi-static indentation loading rate. Predictions are given as to when and where the dislocation will nucleate within the crystal, and what slip mode the nucleated dislocation will take. The critical stress state at the nucleation site is verified by the DFT calculation. The ideal shear strength probed through nanoindentation, which is defined as the CRSS at the site of the first homogeneous dislocation nucleation event, is evaluated. Finally, 3D MD simulations are performed to verify predictive simulations qualitatively.

5.1. Load-displacement response

Indentation is simulated for a frictionless spherical indenter pressed into the (1 1 1) surface of an anisotropic, elastic half-space. The radius of the indenter is 500 Å, the approximate tip radius of a nominally sharp Berkovich indenter used in nanoindentation experiments. Extensive testing is undertaken to assess the effects of geometry of the simulated system, imposed far-field boundary conditions, element type, and node density by comparing with the Hertzian solutions for linear isotropic and anisotropic elastic

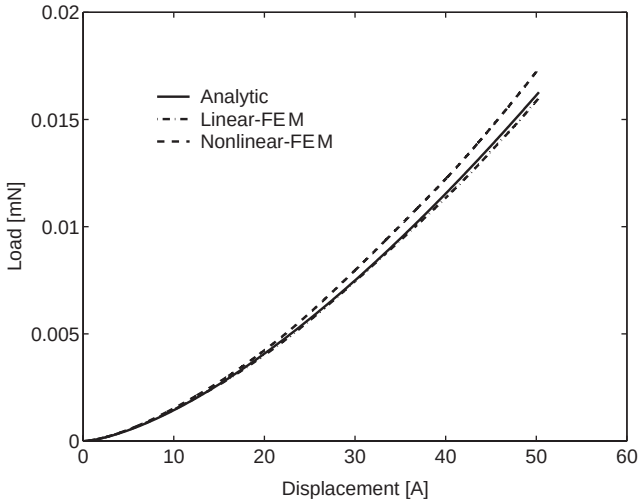

Fig. 11. Load versus displacement curves of nanoindentation by a spherical indenter.

materials. The size of the simulated system is taken to be $3000 \times 3000 \times 6000$ Å. The choice of the elongated system along the indentation direction is based on the study of FEM calculations of Vickers indentation by Giannakopoulos et al. (1994), who showed that the boundary condition error is minimized in this manner. The computational cost can be further reduced considering the three-fold rotation symmetry of the (1 1 1) surface. In the simulation, the displacement along the bottom of the mesh is constrained to be zero, while the displacements of lateral surfaces are unconstrained. The force on the indenter will increase by about 5% if the traction-free boundary condition of lateral surfaces is changed to be fixed (Laursen and Simo, 1992). The graded mesh comprises 8-node linear brick elements. The typical size of elements near the indenter is about 10 Å, and indentation proceeds in displacement-control. Fig. 11 compares the indentation responses predicted by the analytic solution given in Section 3.2, FEM simulations based on linear anisotropic elasticity and on interatomic potential-based hyperelasticity. The FEM simulation based on linear anisotropic elasticity is in good agreement with the analytic solution, while the force on the indenter from the FEM simulation based on interatomic potential-based hyperelasticity is larger due to the non-linear elastic effect generically termed "pressure-hardening", but which has been discovered to be highly dependent on orientation (Ogata et al., 2002). The calculations are terminated at an indentation depth of 50.3 Å, when the onset of dislocation nucleation is first detected via the dislocation nucleation criterion. The corresponding indentation load is about 17.4 μN. Load-controlled nanoindentation experiments (Suresh et al., 1999) on polycrystalline Cu films of different film thicknesses showed that the first burst in the P–h response occurs at a load of 35 ± 10 μN. This discrepancy between the predicted and experimentally determined critical load is mainly due to the idealization of rounded Berkovich indenter tip as a spherical indenter, and/or to various experimental

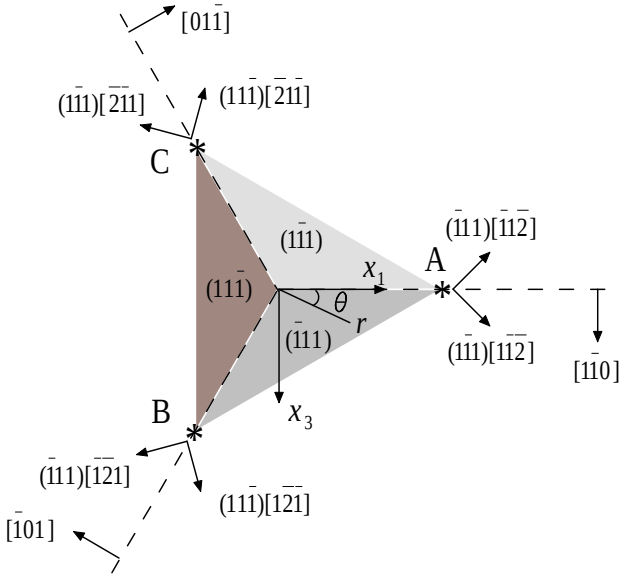

Fig. 12. Illustration of dislocation nucleation sites and the corresponding slip systems: top view of the indented (1 1 1) surface. Some important crystallographic planes and directions are also projected into the (1 1 1) plane.

uncertainties such as estimated tip radius, surface oxidation and strong polycrystalline texture in real films.

5.2. Prediction of dislocation nucleation

The dislocation nucleation sites are identified via the Λ-criterion. Fig. 12 shows the top view of the indented (1 1 1) surface. The global Cartesian coordinate system is the same as that in the linear analysis. For the convenience of positioning nucleation sites, the (r,θ,z) coordinate system is introduced, where (r,θ) are the polar coordinates in the x_1–x_3 plane and the coordinate z is the distance below the (1 1 1) surface. The important crystallographic planes and directions are projected into the (1 1 1) plane as shown in Fig. 12. The (1 1 1) surface has a three-fold rotation symmetry about the [1 1 1] direction. The other three close-packed $\{1\,1\,1\}$-type planes, represented by the shaded triangles in Fig. 12, are positioned symmetrically below the (1 1 1) surface, and at an orientation of 120° with respect to each other about the [1 1 1] loading axis. For 2D indentation discussed in the previous section, the $(1\,1\,\bar{1})$ slip plane is favored for dislocation nucleation due to the kinematic constraints imposed by the 2D nature of the simulation. In contrast, three $\{1\,1\,1\}$-type slip planes beneath the (1 1 1) surface are equivalent in 3D indentation.

Without loss of generality, the critical sites for dislocation nucleation on the $(1\,\bar{1}\,1)$ slip plane are first identified. The corresponding spatial distribution of $\det[\mathbf{Q}(\mathbf{n})]$ is 3D in character, but it is symmetric with respect to the $\theta = 2\pi/3$ plane due to the symmetry

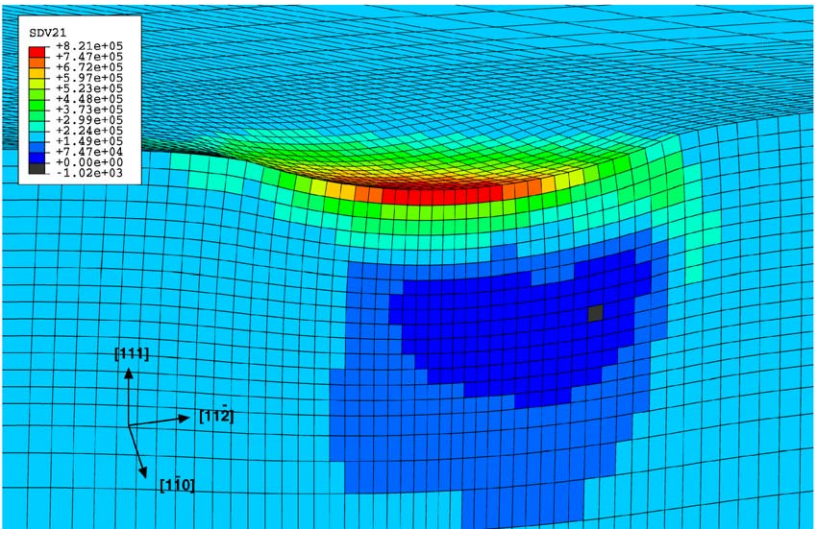

Fig. 13. Contour of det[$\mathbf{Q}(\mathbf{n})$] by 3D FEM simulation, the cross section plane is x_1–x_2 plane.

of the $(1\,\bar{1}\,1)$ slip plane about the $\theta = 2\pi/3$ plane. The distribution of det[$\mathbf{Q}(\mathbf{n})$] within the $\theta = 2\pi/3$ plane presents very similar characteristics to that for the 2D case as shown in Fig. 9. As the detected sites deviate from the $\theta = 2\pi/3$ plane, the spatial distribution of det[$\mathbf{Q}(\mathbf{n})$] changes. Two nucleation sites are identified from the critical elements with vanishing det[$\mathbf{Q}(\mathbf{n})$]. The projected positions of these two critical sites are schematically represented by points A and C in Fig. 12. The contour of det[$\mathbf{Q}(\mathbf{n})$] for the $(1\,\bar{1}\,1)$ slip plane is shown in Fig. 13. The black color element with a small negative value of det[$\mathbf{Q}(\mathbf{n})$] indicates the site of nucleation. One nucleation site within the x_1–x_2 plane ($\theta = 0$) is visible in Fig. 13 and it corresponds to point A in Fig. 12. The in-plane coordinate of this nucleation site (in the undeformed coordinate system) is 92.7 Å below the contact surface and off the central axis by 96.5 Å. For the present indentation simulation (indenter radius $R = 500$ Å and critical penetration depth $h = 50.3$ Å), the nominal contact radius $a = \sqrt{Rh} = 158.6$ Å. Thus, the nucleation sites are $0.58a$ below the contact surface and displaced from the central axis by approximately the same distance, $0.61a$.

The slip directions of the homogeneously nucleated dislocation are predicted by the eigenvector analysis of the corresponding matrix $\mathbf{Q}(\mathbf{n})$. The deformation gradient matrix $\mathbf{F}^{\mathrm{Crit}}$ corresponding to the critical element in Fig. 13 is

$$\mathbf{F}^{\mathrm{Crit}} = \begin{bmatrix} 0.984 & -0.011 & 0.000 \\ -0.115 & 0.920 & 0.005 \\ 0.000 & -0.001 & 1.064 \end{bmatrix}. \tag{27}$$

The Cauchy stress, elastic constant and current slip plane normal are then calculated. The eigenvector analysis predicts that the slip vector $\mathbf{g}$ (in the global coordinate system)

Table 2
Positions and slip systems of homogeneously nucleated dislocations

Nucleation site	Position (r,θ,z)	Slip systems
A	$0.58a, 0, 0.61a$	$(1\,\bar{1}\,1)[1\,\bar{1}\,\bar{2}]$ & $(\bar{1}\,1\,1)[\bar{1}\,1\,\bar{2}]$
B	$0.58a, 2\pi/3, 0.61a$	$(\bar{1}\,1\,1)[\bar{1}\,\bar{2}\,1]$ & $(1\,1\,\bar{1})[1\,\bar{2}\,\bar{1}]$
C	$0.58a, 4\pi/3, 0.61a$	$(1\,1\,\bar{1})[\bar{2}\,1\,\bar{1}]$ & $(1\,\bar{1}\,1)[\bar{2}\,\bar{1}\,1]$

is $[0.630\ 0.346\ 0.695]^{\mathrm{T}}$, while the normalized slip vector calculated from the classical relation gives $\mathbf{g} = \mathbf{F}\mathbf{g}^{\mathrm{o}} = [0.675\ 0.374\ 0.636]^{\mathrm{T}}$, where the initial slip vector $\mathbf{g}^{\mathrm{o}}$ (in the crystal coordinate system) is $[1\,\bar{1}\,\bar{2}]^{\mathrm{T}}$. Accordingly, at the nucleation site A, a Shockley partial slip along the $[1\,\bar{1}\,\bar{2}]$ direction will develop within the $(1\,1\,\bar{1})$ slip plane. For the $(1\,1\,\bar{1})$ slip plane at the nucleation site C, the Shockley partial slip direction is determined to be along the $[\bar{2}\,\bar{1}\,1]$ direction by taking into account the symmetry of the $(1\,1\,\bar{1})$ plane with respect to the $\theta = 2\pi/3$ plane.

Similarly, the nucleation sites and slip modes for the $(\bar{1}\,1\,1)$ and $(1\,\bar{1}\,1)$ slip planes are determined based on three-fold symmetry of the $(1\,1\,1)$ surface. In summary, there are three symmetrically distributed dislocation nucleation sites below the $(1\,1\,1)$ surface, as designated schematically by the points (A, B, C) in Fig. 12. At each site, two slip planes are equally likely to be activated. Table 2 summarizes the positions and slip systems at each nucleation site. In previous studies (Suresh et al., 1999; Gouldstone et al., 2000), the maximum equivalent shear stress criterion is used to identify the dislocation nucleation sites. From the Hertzian contact solution based on linear elasticity (Johnson, 1985), the only potential dislocation nucleation site is along the central axis at a depth of $0.48a$.

5.3. Ideal shear strength of Cu

One of the potential applications of nanoindentation is the experimental characterization of the ideal shear strength of the material. The correlation of the ideal shear strength with the onset of P–h discontinuity has been made by stress analysis from the Hertzian contact solution based on linear isotropic elasticity, see Gerberich et al. (1996) for Si Kiely and Houston (1998) for Au, Suresh et al. (1999) and Gouldstone et al. (2000) for Al and Cu. A recent study by Krenn et al. (2002) gave a better connection between the atomistic and experimental estimates of ideal shear strength of W and Mo by taking into account non-linear elastic effects. The detailed ab initio DFT calculations for affine shear deformation of Cu and Al by Ogata et al. (2002) showed that the ideal shear strength strongly depends on the triaxial stress state. In this subsection, the ideal shear strength of Cu is obtained from the critical shear stress resolved in the Shockley partial slip direction at the dislocation nucleation site. Though the value of ideal shear strength is not uniquely defined and depends on the deformation state at the point of instability, the ideal strength probed through nanoindentation provides a means to quantify this mechanical parameter experimentally.

Substitution of the deformation gradient matrix Eq. (27) into Eq. (7) gives the Cauchy stress in the global coordinate system

$$\boldsymbol{\sigma}^{\text{Mishin}} = \begin{bmatrix} -0.79 & -5.86 & 0.22 \\ -5.86 & -19.38 & 0.49 \\ 0.22 & 0.49 & -4.61 \end{bmatrix} \text{GPa}. \tag{28}$$

Using the same deformation gradient in Eq. (27), the ab initio DFT calculation following the scheme by Ogata et al. (2002) gives the Cauchy stress

$$\boldsymbol{\sigma}^{\text{DFT}} = \begin{bmatrix} -0.59 & -5.90 & 0.21 \\ -5.90 & -19.24 & 0.48 \\ 0.21 & 0.48 & -5.41 \end{bmatrix} \text{GPa}. \tag{29}$$

The agreement between the above two calculations demonstrates the accuracy of quantitative characterization of the critical stress state from FEM simulations via the Mishin potential. The ideal strength, e.g., resolved shear stress in the $(1\,\bar{1}\,1)[1\,\bar{1}\,\bar{2}]$ slip system, is then calculated to be 4.56 GPa, and the corresponding triaxial stress is -8.26 GPa. Compared to the fully relaxed pure shear deformation calculation (the ideal shear strength of 2.16 GPa and triaxial stress of zero) by Ogata et al. (2002), the ideal shear strength probed by nanoindentation is greater by a factor of two, due to the large triaxial stress at the critical site of dislocation nucleation.

5.4. MD simulation

Direct MD simulations conducted for a smaller system at a comparatively high indentation loading rate (about 6 m/s) qualitatively verify the prediction of dislocation nucleation via the Λ-criterion. A spherical indenter with a radius of 50 Å is pressed into the (1 1 1) surface of a Cu cube with an approximate side length of 100 Å. Figs. 14(a) and (b) show the bottom view (along [1 1 1] direction) and the side view (along $[1\,1\,\bar{2}]$ direction) of three dislocation embryos nucleated on the inclined $\{1\,1\,1\}$-type slip planes beneath the surface, respectively. The perfectly coordinated atoms within the bulk ($N = 12$) have been removed from the images for clarity, such that only surface and imperfectly coordinated atoms are visible. The green atom in Fig. 14(a) represents the first contact point between the indenter and the (1 1 1) surface. In contrast to the formation of a straight dislocation line in 2D simulation, the dislocation embryo nucleates as a group of atoms, and will expand into a partial dislocation loop. Embryo size is indicative of the sequence of embryo nucleation, with larger embryos nucleating at earlier time increments. In the MD simulation, it is observed that the largest embryo shown in Figs. 14(a) and (b) first nucleates along the $(1\,\bar{1}\,1)$ plane. Then, the medium-sized embryo nucleates along the $(\bar{1}\,1\,1)$ plane almost simultaneously. The site and slip mode of this second embryo are symmetric to those of the first embryo, with respect to x_1–x_2 plane. In the time increment shown in Figs. 14(a) and (b), the smallest embryo has just nucleated. It will expand within the same $(1\,\bar{1}\,1)$ slip

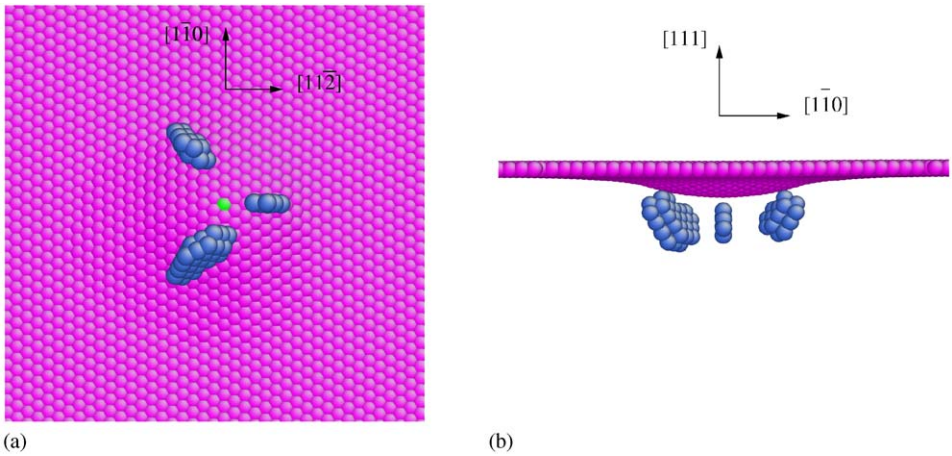

Fig. 14. MD simulation of nanoindentation by a spherical indenter: atomic structure of homogeneously nucleated dislocations beneath the (1 1 1) surface: (a) bottom view along the [1 1 1] direction; (b) side view along the [1 1 $\bar{2}$] direction. The indenter first contacts the green atom.

plane as the first embryo and coalesce. These three, symmetrically distributed nucleation sites observed in MD simulations agree with predictions from FEM simulations via the Λ-criterion. The same distribution of nucleation sites and structure of dislocation embryos were also observed by Kelchner et al. (1998) in MD simulations of indentation on the (1 1 1) surface of Au. They further identified the slip vector via the centrosymmetry parameter. For example, they observed that the slip on the ($\bar{1}$ 1 1) plane is in the [$\bar{1}$ $\bar{2}$ 1] direction, which agrees with the prediction based on the eigenvector analysis of the Λ-criterion. Thus, the important features of the homogeneously nucleated dislocations predicted by FEM calculations via the Λ-criterion qualitatively agree with MD simulations, though the quantitative state including the critical indentation load and stress field for dislocation nucleation differ due to discrepancies in loading rate and system size.

In MD simulations for Cu given above and for Au by Kelchner et al. (1998), it is observed that at the very early stage of dislocation nucleation, the glide process always occurs along two of the three inclined {1 1 1}-type slip planes. A three fold symmetric defect structure is never obtained. The loss of the (1 1 1) surface three-fold symmetry can be explained by examining the distribution and slip characters of nucleated dislocations shown in Figs. 14(a) and (b) with reference to the predictions given in Table 2 and Fig. 12. Though there exist three equivalent dislocation nucleation sites and two possible slip planes at each site, the first nucleated two dislocations along the (1 $\bar{1}$ 1) and ($\bar{1}$ 1 1) slip planes occupy each of two possible nucleation sites for the (1 1 $\bar{1}$) slip plane, respectively. Moreover, the two nucleated dislocations with symmetric sites and slip modes could accommodate geometrically the deformation imposed by the indenter penetration. Accordingly, the subsequent activation of the glide process along the (1 1 $\bar{1}$) slip plane is likely to be suppressed, as observed in MD simulations.

6. Discussion and summary

Nanoindentation-induced homogeneous dislocation nucleation in single crystal copper has been analyzed within the framework of hyperelasticity with the Cauchy–Born hypothesis. Homogeneous dislocation nucleation is interpreted as a strain localization event triggered by elastic instability in a perfect crystal at finite strain. Since the constitutive model of interatomic potential-based hyperelasticity incorporates the key crystal properties such as crystalline anisotropy and nonlinear elastic effects, it is well-suited to the study of defect nucleation at the continuum level while maintaining fidelity with the underlying atomistic response. The efficiency of the finite element formulation permits the simulation of significantly larger systems than would otherwise be possible. However, care must be taken in applying this approach for predictive modeling of defect nucleation because the Cauchy–Born hypothesis is only valid when the spatial variation of the continuum deformation field is gradual on the atomic scale. For problems such as dislocation nucleation at an atomistically sharp crack tip (Rice, 1992), the large strain gradient near the crack tip necessitates the use of the quasi-continuum or direct atomistic methods which can account explicitly for non-local effects. However, in the present study of a relatively slowly varying deformation field imposed by a 50 nm-scale indenter radius, interatomic potential-based hyperelasticity is efficiently and effectively utilized.

As the present simulations idealize indentation normal to an atomically flat surface, it follows that the dislocation nucleates homogeneously within the crystal and moves/grows to approach the free surface. This atomistic process is in contrast with nanoindentation-induced heterogeneous dislocation nucleation from surface steps (Kiely and Houston, 1998; Zimmerman et al., 2001), a process subject to a much lower energy barrier that may significantly decrease the simulated or experimentally measured critical load. Furthermore, we restricted the present dislocation nucleation study to the idealized limit of behavior at 0 K, and in the absence of specific effects of thermally activated processes. As a result, the ideal shear strength obtained via 3D indentation simulation represents the mechanical threshold for nanoindentation-induced dislocation nucleation. The effect of thermal motion on homogeneous nucleation of dislocation loops under a simple shear stress state has been studied by Xu and Argon (2001) using a variational boundary integral method to determine the saddle point configuration and the corresponding activation energy. They found that for perfect crystals such as Au, Cu, Al and Si, the energy barriers are far too high for thermal motion to play a significant role in dislocation nucleation, even under applied shear stress levels equal to half of the ideal simple shear strength. The activation energy for homogeneous dislocation nucleation beneath the nanoindenter could be evaluated using the same scheme as Xu and Argon (2001). FEM simulations of nanoindentation using interatomic potential-based hyperelasticity will provide a more realistic stress state beneath the nanoindenter, rather than using a simple shear stress state as an input for activation energy calculation.

We conclude by noting that the study of defect nucleation within the framework of hyperelasticity is not limited to simple FCC lattices and bulk homogeneous material systems. Further extension of interatomic potential-based hyperelasticity has been made to other type of lattices, e.g., Tadmor et al. (1999b) and Smith et al. (2001)

for nonsymmorphic crystal lattices such as diamond cubic Si, Arroyo and Belytschko (2002) for a one-atom thick carbon nanotubes, etc. Furthermore, the instability analysis we employed to predict defect nucleation within the bulk can also be generalized to study surface and interface instabilities, as well as homogeneous defect nucleation at coherent grain boundaries with the aid of a generalized instability criterion at interfaces (Needleman and Ortiz, 1991). Such extensions will further demonstrate the applicability of defect nucleation analyses within the framework of hyperelasticity, and will enable the study of a wide range of phenomena at the continuum level, while maintaining explicitly the atomistic interactions which govern the mechanical response.

Acknowledgements

This work was supported by the Defense University Research Initiative on NanoTechnology (DURINT) on "Damage and Failure Resistant Nanostructured Materials and Interfacial Coatings" which is funded at MIT by the Office of Naval Research. T.Z., S.Y. acknowledge support by NSF/KDI/DMR, AFOSR and Lawrence Livermore National Laboratory. J.L. acknowledges support by Honda R& D Co., Ltd. and the OSU Transportation Research Endowment Program. K.J.V.V. acknowledges the support of the National Defense Science and Engineering Graduate Fellowship program. S.O. acknowledges support by Murata-Kaigai-Ryugaku-Syougakukai fellowship.

Appendix A. Stroh formalism for generalized 2D anisotropic elasticity

Basic equations for Stroh formalism, which are used for deriving 2D and 3D analytic indentation solutions, are given in this appendix (Ting, 1996). A general solution for displacement $\mathbf{u}$ and stress function $\mathbf{\Phi}$ is given by

$$\mathbf{u} = \mathbf{A}\mathbf{f}(z) + \overline{\mathbf{A}\mathbf{f}(z)}, \tag{A.1}$$

$$\mathbf{\Phi} = \mathbf{B}\mathbf{f}(z) + \overline{\mathbf{B}\mathbf{f}(z)}, \tag{A.2}$$

where

$$\mathbf{A} = [\mathbf{a}_1 \ \mathbf{a}_2 \ \mathbf{a}_3], \tag{A.3}$$

$$\mathbf{B} = [\mathbf{b}_1 \ \mathbf{b}_2 \ \mathbf{b}_3], \tag{A.4}$$

$$\mathbf{f} = [f_1(z_1) \ f_2(z_2) \ f_3(z_3)]^{\mathrm{T}}, \tag{A.5}$$

$$z_\alpha = x + p_\alpha y, \quad \alpha = 1, 2, 3, \tag{A.6}$$

$\mathbf{f}$ is a complex function vector to be determined by satisfying the boundary conditions of the problem considered. Given the elastic constants tensor C_{ijkl} which is expressed in the global coordinates, p_α and $\mathbf{a}_\alpha$ can determined by solving the following eigenvalue problem

$$[\mathbf{Q} + (\mathbf{R} + \mathbf{R}^{\mathrm{T}})p + \mathbf{T}p^2]\mathbf{a} = 0, \tag{A.7}$$

where

$$Q_{ik} = C_{i1k1}, \quad R_{ik} = C_{i1k2} \quad \text{and} \quad T_{ik} = C_{i2k2}. \tag{A.8}$$

The non-zero solution of $\mathbf{a}$ requires that

$$\det[\mathbf{Q} + (\mathbf{R} + \mathbf{R}^{\mathrm{T}})p + \mathbf{T}p^2] = 0. \tag{A.9}$$

Eq. (A.9) has six roots which form three conjugate pairs. The root p_α has a positive imaginary part, and thus $\mathbf{b}_\alpha$ is obtained by

$$\mathbf{b}_\alpha = (\mathbf{R}^{\mathrm{T}} + p_\alpha \mathbf{T})\mathbf{a}_\alpha. \tag{A.10}$$

The stresses are given by

$$\{\sigma_{2j}\} = 2\,\mathrm{Re}\sum_{\alpha=1}^{3} \mathbf{b}_\alpha f'_\alpha(z_\alpha), \tag{A.11}$$

$$\{\sigma_{1j}\} = -2\,\mathrm{Re}\sum_{\alpha=1}^{3} \mathbf{b}_\alpha p_\alpha f'_\alpha(z_\alpha). \tag{A.12}$$

The impedance matrix $\mathbf{M}$ appears in the 2D indentation solution. It is defined by

$$\mathbf{M} = -i\mathbf{B}\mathbf{A}^{-1}. \tag{A.13}$$

$\mathbf{M}$ is a Hermitian matrix and independent of how $\mathbf{a}_\alpha$ and $\mathbf{b}_\alpha$ are normalized. The Barnett–Lothe tensor $\hat{\mathbf{L}}$ is employed in deriving the 3D indentation solution. It is defined by

$$\hat{\mathbf{L}} = -2i\mathbf{B}\mathbf{B}^{\mathrm{T}}, \tag{A.14}$$

where the vectors $\mathbf{a}_\alpha$ and $\mathbf{b}_\alpha$ are normalized by

$$2\mathbf{a}_\alpha \cdot \mathbf{b}_\alpha = 1. \tag{A.15}$$

References

ABAQUS, 2001. Reference Manuals. Hibbitt, Karlsson and Sorensen Inc., Pawtucket, R.I.

Abeyaratne, R., Bhattacharya, K., Knowles, J.K., 2001. Strain-energy functions with multiple local minima: modeling phase transformations using finite thermo-elasticity. In: Fu, Y., Ogden, R.W. (Eds.), Nonlinear Elasticity: Theory and Applications. Cambridge University Press, Cambridge, pp. 433–480.

Ackland, G.J., Bacon, D.J., Calder, A.F., Harry, T., 1997. Computer simulation of point defect properties in dilute Fe–Cu alloy using a many-body interatomic potential. Philos. Mag. A 75, 713–732.

Allen, M.P., Tildesley, D.J., 1987. Computer Simulation of Liquids. Clarendon Press, Oxford.

Arroyo, M., Belytschko, T., 2002. An atomistic-based finite deformation membrane for single layer crystalline films. J. Mech. Phys. Solids 50, 1941–1977.

Asaro, R.J., 1983. Crystal plasticity. J. Appl. Mech. 50, 921–934.

Barnett, D.M., Lothe, J., 1975. Line force loadings on anisotropic half-spaces and wedges. Phys. Norv. 8, 13–22.

Born, M., Huang, K., 1956. Dynamical Theory of Crystal Lattices. Clarendon Press, Oxford.

Cheung, K.S., Yip, S., 1991. Atomic-level stress in an inhomogeneous system. J. Appl. Phys. 70, 5688–5690.

Corcoran, S.G., Colton, R.J., Lilleodden, E.T., Gerberich, W.W., 1997. Anomalous plastic deformation at surfaces: nanoindentation of gold single crystals. Phys. Rev. B 55, R16057–R16060.

Daw, M.S., Baskes, M.I., 1983. Semiempirical, quantum mechanical calculation of hydrogen embrittlement in metals. Phys. Rev. Lett. 50, 1285–1288.

Ericksen, J.L., 1984. The Cauchy and Born hypotheses for crystals. In: Gurtin, M.E. (Ed.), Phase Transformations and Material Instabilities in Solids. Academic Press, New York, pp. 61–78.

Fan, C.W., Hwu, C.B., 1996. Punch problems for an anisotropic elastic half-plane. J. Appl. Mech. 63, 69–76.

Fivel, M.C., Robertson, C.F., Canova, G.R., Boulanger, L., 1998. Three-dimensional modeling of indent-induced platic zone at a mesoscale. Acta Mater. 46, 6183–6194.

Gao, H., Klein, P., 1998. Numerical simulation of crack growth in an isotropic solid with randomized internal cohesive bonds. J. Mech. Phys. Solids 46, 187–218.

Gerberich, W.W., Nelson, J.C., Lilleodden, E.T., Anderson, P., Wyrobek, J.T., 1996. Indentation induced dislocation nucleation: the initial yield point. Acta Mater. 44, 3585–3598.

Giannakopoulos, A.E., Larsson, P.L., Vestergaard, R., 1994. Analysis of vickers indentation. Int. J. Solid Struct. 31, 2679–2708.

Gouldstone, A., Koh, H.J., Zeng, K.Y., Giannakopoulos, A.E., Suresh, S., 2000. Discrete and continuous deformation during nanoindentation of thin films. Acta Mater. 48, 2277–2295.

Gouldstone, A., Van Vliet, K.J., Suresh, S., 2001. Nanoindentation: simulation of defect nucleation in a crystal. Nature 411, 656–656.

Hill, R., 1962. Acceleration waves in solids. J. Mech. Phys. Solids 10, 1–16.

Hill, R., 1975. On the elasticity and stability of perfect crystals at finite strain. Math. Proc. Cambridge Philos. Soc. 77, 225–240.

Johnson, K.L., 1985. Contact Mechanics. Cambridge University Press, Cambridge.

Kelchner, C.L., Plimpton, S.J., Hamilton, J.C., 1998. Dislocation nucleation and defect structure during surface indentation. Phys. Rev. B 58, 11085–11088.

Kiely, J.D., Houston, J.E., 1998. Nanomechanical properties of Au (111), (001), and (110) surfaces. Phys. Rev. B 57, 12588–12594.

Klein, P., Gao, H., 1998. Crack nucleation and growth as strain localization in a virtual-bond continuum. Eng. Fract. Mech. 61, 21–48.

Knap, J., Ortiz, M., 2001. An analysis of the quasicontinuum method. J. Mech. Phys. Solids 49, 1899–1923.

Krenn, C.R., Roundy, D., Morris, J.W., Cohen, M.L., 2001. The non-linear elastic behavior and ideal shear strength of Al and Cu. Mater. Sci. Eng. A 317, 44–48.

Krenn, C.R., Roundy, D., Cohen, M.L., Chrzan, D.C., Morris, J.W., 2002. Connecting atomistic and experimental estimates of ideal strength. Phys. Rev. B 65, 134111.

Laursen, T.A., Simo, J.C., 1992. A study of the mechanics of microindentation using finite elements. J. Mater. Res. 7, 618–626.

Li, J., 2003. Atomeye: an efficient atomistic configuration viewer. Modelling Simul. Mater. Sci. Eng. 11, 173–177.

Li, J., Van Vliet, K.J., Zhu, T., Yip, S., Suresh, S., 2002. Atomistic mechanisms governing elastic limit and incipient plasticity in crystals. Nature 418, 307–310.

Mishin, Y., Farkas, D., Mehl, M.J., Papaconstantopoulos, D.A., 1999. Interatomic potentials for monoatomic metals from experimental data and ab initio calculations. Phys. Rev. B 59, 3393–3407.

Mishin, Y., Mehl, M.J., Papaconstantopoulos, D.A., Voter, A.F., Kress, J.D., 2001. Structural stability and lattice defects in copper: ab initio, tight-binding, and embedded-atom calculations. Phys. Rev. B 63, 224106.

Needleman, A., Ortiz, M., 1991. Effect of boundaries and interfaces on shear-band localization. Int. J. Solid Struct. 28, 859–877.

Ogata, S., Li, J., Yip, S., 2002. Ideal pure shear strength of aluminum and copper. Science 298, 807–811.

Ogden, R.W., 1984. Non-linear Elastic Deformations. Wiley, New York.

Oliver, W.C., Pharr, G.M., 1992. An improved technique for determining hardness and elastic modulus using load and displacement sensing indentation experiments. J. Mater. Res. 7, 1564–1583.

Ortiz, M., Phillips, R., 1999. Nanomechanics of defects in solids. In: Wu, T.Y., van der Giessen, E. (Eds.), Advances in Applied Mechanics, Vol. 36. Academic Press, New York, pp. 1–79.

Page, T.F., Oliver, W.C., McHargue, C.J., 1992. The deformation-behavior of ceramic crystals subjected to very low load (nano)indentations. J. Mater. Res. 7, 450–473.

Rice, J.R., 1976. The localization of plastic deformation. In: Koiter, W.T. (Ed.), Theoretical and Applied Mechanics. North-Holland, Amsterdam, pp. 207–220.

Rice, J.R., 1992. Dislocation nucleation from a crack tip: an analysis based on the peierls concept. J. Mech. Phys. Solids 40, 239–271.

Shenoy, V.B., Miller, R., Tadmor, E.B., Rodney, D., Phillips, R., Oriz, M., 1999. An adaptive finite element approach to atomic-scale mechanics—the quasicontinuum method. J. Mech. Phys. Solids 47, 611–642.

Shenoy, V.B., Phillips, R., Tadmor, E.B., 2000. Nucleation of dislocations beneath a plane strain indenter. J. Mech. Phys. Solids 48, 649–673.

Smith, G.S., Tadmor, E.B., Bernstein, N., Kaxiras, E., 2001. Multiscale simulations of silicon nanoindentation. Acta Mater. 49, 4089–4101.

Suresh, S., Nieh, T.G., Choi, B.W., 1999. Nano-indentation of copper thin films on silicon substrates. Scripta Mater. 41, 951–957.

Swadener, J.G., Pharr, G.M., 2001. Indentation of elastically anisotropic half-spaces by cones and parabolae of revolution. Philos. Mag. A 81, 447–466.

Tadmor, E.B., Ortiz, M., Phillips, R., 1996. Quasicontinuum analysis of defects in solids. Philos. Mag. A 73, 1529–1563.

Tadmor, E.B., Miller, R., Phillips, R., Ortiz, M., 1999a. Nanoindentation and incipient plasticity. J Mater. Res. 14, 2233–2250.

Tadmor, E.B., Smith, G.S., Bernstein, N., Kaxiras, E., 1999b. Mixed finite element and atomistic formulation for complex crystals. Phys. Rev. B 59, 235–245.

Ting, T.C.T., 1996. Anisotropic Elasticity: Theory and Applications. Oxford University Press, New York.

Van Vliet, K.J., Li, J., Zhu, T., Yip, S., Suresh, S., 2003. Quantifying the early stages of plasticity through nanoscale experiments and simulations. Phys. Rev. B 67, 104105.

Vlassak, J.J., Nix, W.D., 1993. Indentation modulus of elastically anisotropic half-spaces. Philos. Mag. A 67, 1045–1056.

Vlassak, J.J., Nix, W.D., 1994. Measuring the elastic properties of anisotropic materials by means of indentation experiments. J. Mech. Phys. Solids 42, 1223–1245.

Wallace, D.C., 1972. Thermodynamics of Crystals. Wiley, New York.

Willis, J.R., 1966. Hertzian contact of anisotropic bodies. J. Mech. Phys. Solids 14, 163–176.

Xu, G., Argon, A.S., 2001. Energetics of homogeneous nucleation of dislocation loops under a simple shear stress in perfect crystals. Mater. Sci. Eng. A 319–321, 144–147.

Zhang, P., Klein, P., Huang, Y., Gao, H., Wu, P.D., 2002. Numerical simulation of cohesive fracture by the virtual-internal-bond model. Comp. Model. Eng. Sci. 3, 263–277.

Zimmerman, J.A., Kelchner, C.L., Klein, P.A., Hamilton, J.C., Foiles, S.M., 2001. Surface step effects on nanoindentation. Phys. Rev. Lett. 87, 165507.